Physik-Department

Simulation of Frictional Cooling

Diplomarbeit
von

Christian Blume

Technische Universität
München

Abstract

Achieving particle beams with small phase space volumes is a great challenge in high energy particle physics. Different cooling techniques have been developed for various particle types and accelerator schemes. However, for novel accelerator concepts like that of a Muon Collider new cooling techniques have to be investigated. The concept of Frictional Cooling holds promise to decrease the emittance of a beam of heavy charged unstable particles significantly on a timescale smaller than their lifetime.

The Frictional Cooling Demonstration (FCD) experiment at the Max-Planck-Institute for Physics, Munich, aims to demonstrate the principle on protons. In this work, a full Monte Carlo simulation of the experiment based on the Geant4 framework is presented and discussed. The simulation validates that the experiment can demonstrate the principles of Frictional Cooling. Predictions for data are made. Furthermore, a simulation of a muon cooling cell used in a possible Muon Collider is undertaken. It will be shown that the simulated muon cooling channel strongly reduces the emittance of a beam of muons on a tiny timescale.

Contents

1 Introduction **2**

2 The Idea of Frictional Cooling **5**

3 Validation of the Monte Carlo Simulation **9**
3.1 Geant4 . . . 9
3.2 Energy Loss . . . 10
3.3 Muonium and Hydrogen Formation . . . 11
3.4 Particle Decay . . . 13
3.5 Muon Capture . . . 14
3.6 Simulation of an exemplary Gas Cell . . . 16

4 Simulation of the FCD Experiment **21**
4.1 Experimental Setup . . . 21
4.2 Electric Field . . . 22
4.3 Magnetic Field . . . 24
4.4 Proton Source . . . 26
4.5 Simulation Results . . . 27
4.5.1 Conditions . . . 27
4.5.2 Kinetic Energy . . . 28
4.5.3 Acceptance in the Detector . . . 32
4.5.4 Equilibrium Energy . . . 35

5 Simulation of a Muon Cooling Channel **39**
5.1 Outline of a Muon Collider Scheme . . . 39
5.2 Muon Cooling . . . 40
5.2.1 The Channel . . . 40
5.2.2 Single Particles . . . 42
5.2.3 Equilibrium Energy . . . 45
5.2.4 A Muon Beam . . . 46
5.2.5 Luminosity . . . 49
5.3 Challenges . . . 51

6 Conclusions **52**

References **54**

Chapter 1

Introduction

In order to understand the fundamental constituents of matter, physicists collide particles at high energies. The luminosity of a particle beam is proportional to the number of particles per unit area and unit time. Therefore, the probability to measure collisions between single particles when colliding particle beams increases as the luminosity increases.

In order to reach high luminosities in particle colliders it is favorable to decrease the phase space volume the beam occupies. The design luminosity L [1] is defined as

$$L = fn\frac{N^2}{2\pi\beta^*\epsilon_T} \tag{1.1}$$

where f denotes the revolution frequency, n the number of bunches in the collider, N the number of muons per bunch, β^* the beta function at the interaction point and ϵ_T the average normalized transverse emittance of the beam. ϵ_T is a quantity representing the four-dimensional phase space volume the beam occupies which is defined as

$$\epsilon_\mathrm{T} = \frac{1}{2\pi mc} \cdot \left(\sigma_\mathrm{x}\sigma_\mathrm{p_x} + \sigma_\mathrm{y}\sigma_\mathrm{p_y}\right) \tag{1.2}$$

where m is the rest mass of the particle, c is the speed of light, σ_x and σ_y are the spatial standard deviations of the beam, and $\sigma_\mathrm{p_x}$ and $\sigma_\mathrm{p_y}$ are its standard deviations of the momentum components. The definition in eq. (1.2) is a simplified representation of the phase space volume since it does not take any correlations between the distributions of its ingredients into account. However, this estimate is conservative because any correlations would decrease the emittance.

Reducing the emittance of a particle beam is referred to as cooling. In most current collider structures particles such as electrons, protons or ions are cooled via electron cooling [2] or stochastic cooling [3] and inserted into ring

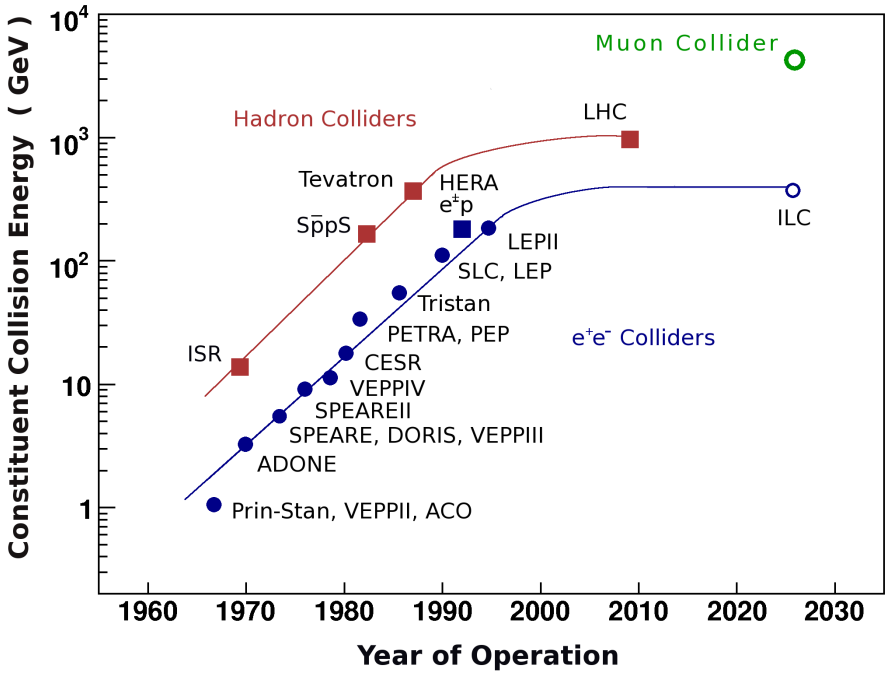

Figure 1.1: The Livingston plot including the Muon Collider.

accelerators where they are collimated by electric and magnetic fields. These techniques are able to reduce the occupied phase space volume strongly. For every stable charged particle this cooling scheme works efficiently. However, novel cooling techniques need to be developed in order to collide unstable particles since a significant emittance reduction on a time scale comparable to their lifetimes has to take place.

This work addresses the cooling of muons. The muon is 206 times heavier than its leptonic brother, the electron. Thus, colliding muons instead of electrons would lead to a highly suppressed energy loss due to synchrotron radiation E_{synch} since

$$E_{\text{synch}} \propto \left(\frac{E}{m}\right)^4 \tag{1.3}$$

where m denotes the mass of the particle and E its kinetic energy. Using existing collider structures like the LHC center of mass energies of several TeV are conceivable [4].

Furthermore, the muon is a lepton and so is an elementary particle. In contrast to protons where its constituents, quarks and gluons, share its mo-

mentum, muons are point-like particles so that the collision energy can be determined very precisely. Thus, the entire particle energy enters in the collision of muons, in contrast to protons where on average only a small fraction contributes.

In fig. 1.1 the Livingston plot is shown. Outlined is the constituent collision energy versus the year of operation for hadronic, e^+e^- colliders and HERA ($e^{\pm}p$). It can be seen that a saturation effect in energy occurs. Novel collider structures such as a Muon Collider would break this trend and lead to constituent energies well above the 1 TeV border.

Additionally, muon beams that occupy small phase space volumes might also be very suitable for other applications. An example would be the well understood flux of neutrinos from muon decays that could be used to perform oscillation experiments with high data rates [5]. Also muons at the low energy regime have a wide range of physics applications [6].

The muon decays with a mean life time of 2.2 μs. The challenge to reduce the phase space volume of a muon beam significantly on this time scale can be solved by applying the concept of Frictional Cooling. First experiments [7, 8] were undertaken to demonstrate the principle of this new concept. The results were promising and motivate further research.

❖ ❖ ❖

This work is divided into six chapters. Chapter 2 describes the idea of Frictional Cooling. Chapter 3 validates the Monte Carlo simulation used to demonstrate and prove the principles of Frictional Cooling. In Chapter 4 the Frictional Cooling Demonstration (FCD) experiment currently developed at the Max-Planck-Institute for Physics, Munich, is introduced and simulation results are given and interpreted.

Chapter 5 presents the simulation of a muon cooling channel used in a possible Muon Collider structure and gives an estimate of the achievable luminosity. Finally, in the last chapter, conclusions and motivation for further research are given.

Chapter 2

The Idea of Frictional Cooling

Frictional Cooling can be understood as the cooling of a beam of charged particles by moderation in matter and simultaneous acceleration in an electric field. The motivation of Frictional Cooling is being able to reduce the overall phase space volume of a particle beam by several orders of magnitude on a timescale smaller than the mean lifetimes of the particles. Frictional Cooling holds promise to reduce the total emittance up to the limit of multiple scattering.

The principle of Frictional Cooling makes use of the stopping power $\mathrm{d}T/\mathrm{d}x$ that heavy charged particles experience while traversing through a medium. Stopping power is the energy loss $\mathrm{d}T$ per distance $\mathrm{d}x$. The stopping power curve normalized by the density ρ for positively charged muons in Helium is shown in fig. 2.1. Unfortunately, reliable data for muons are not available yet. Therefore, the plot in fig. 2.1 is obtained by scaling the empirically well known stopping power curve for protons taken from the NIST [9] tables. This is done by applying velocity scaling [10] on the cross-sections for energy loss that hold

$$\sigma_\mu(T_\mu) = \sigma_\mathrm{p}(T_\mathrm{p}/M) \tag{2.1}$$

where $M = m_\mathrm{p}/m_\mu = 8.87$ denotes the quotient of proton and muon mass respectively and T_p and T_μ their kinetic energies. Thus, the stopping power curve scales the same.

The region where the principle of Frictional Cooling takes place is from zero energy until the stopping power and the effective energy gain from a constant accelerating force cross on the right side of the ionization peak. In this region the muon either loses energy if it is still above the equilibrium energy or gains energy if it is below. This implies that no matter what energy they are starting at in this region, they all end up at equilibrium energy. Slow particles get accelerated, fast ones get decelerated.

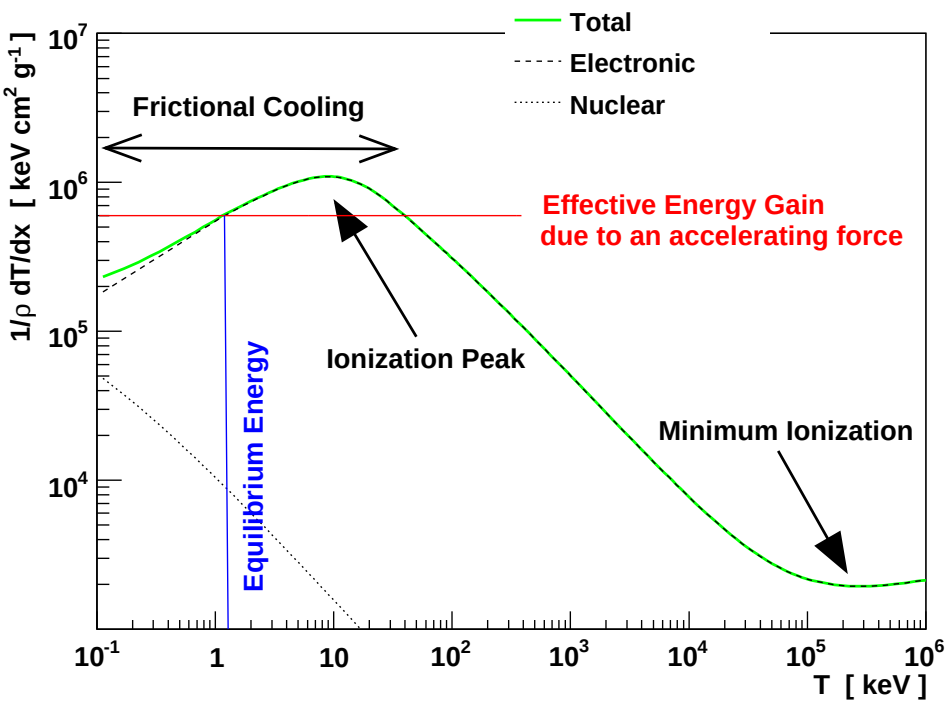

Figure 2.1: Stopping power curve for positively charged muons in Helium. Electronic, nuclear as well as the total stopping power are outlined.

Particles having energies above the crossing point cannot be cooled with a simple constant accelerating force since they gain more energy than they lose. In order to be able to also cool those muons one has to introduce crossed electric and magnetic fields (see chapter 5).

The equilibrium energy is found to be in a region where the stopping power is approximately proportional to the square root of the energy which yields

$$\frac{\mathrm{d}T}{\mathrm{d}x} \propto v \tag{2.2}$$

Frictional Cooling has a simple analog in nature, the free fall in the atmosphere. The constant force of gravity is opposed by the drag force imposed by friction on the falling object that is proportional to the square of the velocity. As a result the object reaches an equilibrium kinetic energy because the forces balance each other. As an accelerating force for charged particles we will make use of the Lorentz-Force

$$\vec{F}_{\mathrm{L}}(\vec{x}) = q\left(\vec{E}(\vec{x}) + \vec{v} \times \vec{B}(\vec{x})\right) \tag{2.3}$$

where q denotes the charge of the particle, $\vec{E}$ the electric field and $\vec{B}$ the magnetic field. For the balance between the average energy loss due to the stopping of the medium and the Lorentz-force follows

$$\vec{F}_{\mathrm{L}}(\vec{x}) \stackrel{!}{=} \frac{\mathrm{d}T}{\mathrm{d}x}\hat{v} \tag{2.4}$$

When $T = \mathcal{O}(1\ \mathrm{keV})$ we refer to the mean energy of a bunch of muons as an equilibrium energy T_{eq} when eq. (2.4) holds.

When a muon, or another heavy charged particle such as the proton, travels through a gaseous medium several processes contribute to the overall loss of kinetic energy. These processes are ionization, excitation, charge exchange and nuclear scattering. The first three are referred to as electronic energy loss and the last as nuclear energy loss. Furthermore, particles at low energies elastically scatter from nuclei due to Coulomb scattering which minimally changes the energy of the incident particle but alters the direction of movement. This process is referred to as multiple scattering. A large region of the stopping power curve from approximately $T = 100$ keV to several GeV is well described by the Bethe-Bloch-Equation [11]. For muons, the minimum ionization takes place at approximately $T = 200$ MeV (see fig. 2.1). In regions lower than the minimum ionization a dependence of approximately $1/v^2$ whereas only a logarithmic increase at higher energies is observed. For a full description of the stopping and range of elementary particles and ions in matter one may consider [12].

The ionization peak occurs at approximately 10 keV where $v = \mathcal{O}(\alpha \cdot c)$ where v is the particle's velocity, c is the speed of light and $\alpha = \frac{1}{137}$ is the fine structure constant. The muons velocity v_μ at 10 keV is calculated as

$$v_\mu = \sqrt{2\frac{T_\mu}{m_\mu}} = 0.014\mathrm{c} \tag{2.5}$$

with $m_\mu = 105.658\ \mathrm{MeV/c^2}$. The first ionization energy of Helium is $T_e = 24.6$ eV. The velocity v_{e} of a valence electron is estimated as

$$v_{\mathrm{e}} = \sqrt{2\frac{T_{\mathrm{e}}}{m_{\mathrm{e}}}} = 0.01\mathrm{c} \tag{2.6}$$

with $m_{\mathrm{e}} = 0.511\ \mathrm{MeV/c^2}$. The relative velocities of the valence electrons of the Helium atoms become comparable to the velocity of the incident muon. Thus, the maximum transferable energy to an electron from the incident muon becomes maximal.

The principle of Frictional Cooling operates in a low kinetic energy regime which has not been deeply studied. Many critical issues must be investigated

and their influences understood in detail. For example, charge exchange processes or the capture of negatively charged muons by the atoms of the medium. These subjects will be outlined and discussed in the following chapters.

Chapter 3

Validation of the Monte Carlo Simulation

In this chapter the Monte Carlo simulation based on the Geant4 [13, 14] framework is validated. The processes are outlined and important cross-sections are discussed. Additionally, a simulation of an exemplary gas cell with homogeneous electromagnetic fields is presented.

3.1 Geant4

Geant4 is a framework developed at CERN and based on C++ which allows the simulation of the passage of particles through matter. It was originally designed to describe processes in high energy particle physics. Recently physicists started to implement low energy physics processes [15] into Geant4. It is now possible to simulate the energy loss of particles to the keV range and lower. This simulation program uses Geant4 for tracking, to calculate the energy loss [16–18] and the spatial displacement [19]. For heavy charged elementary particles, as muons and protons, the classes *G4hLowEnergyIonisation* and *G4MultipleScattering* are instantiated in the Geant4 physics list to determine the energy loss end the spatial displacement respectively.

However, special processes important for the Frictional Cooling scheme such as the decay of particles, the effect of Hydrogen (protons) and Muonium (muons) formation, and the capture of negatively charged muons by medium atoms (muon capture) were implemented additionally. Also, the event management was adjusted to meet the requirements. The movement of particles in electric as well as magnetic fields is determined by a 4-th order Runge-Kutta-Method.

A documentation of the simulation program (using Geant4 version 4.9.0)

can be found under http://www.mpp.mpg.de/∼cblume/fcdSimDoc/. The simulation was written and tested for protons and positively charged muons traversing through Helium, Hydrogen, Nitrogen and Argon as well as for negatively charged muons in Helium and Hydrogen. The program structure was developed to be extendable so that new particles, materials or processes can be easily added.

3.2 Energy Loss

One of the most important issues of the Monte Carlo simulation is the energy loss of protons and muons while traversing through a gaseous medium. The comparison between the simulated [14] and experimental stopping power taken from the NIST tables for Helium and Hydrogen is shown in fig. 3.1. The experimental data for μ^+ are once more retrieved due to scaling the well known data for protons via velocity scaling.

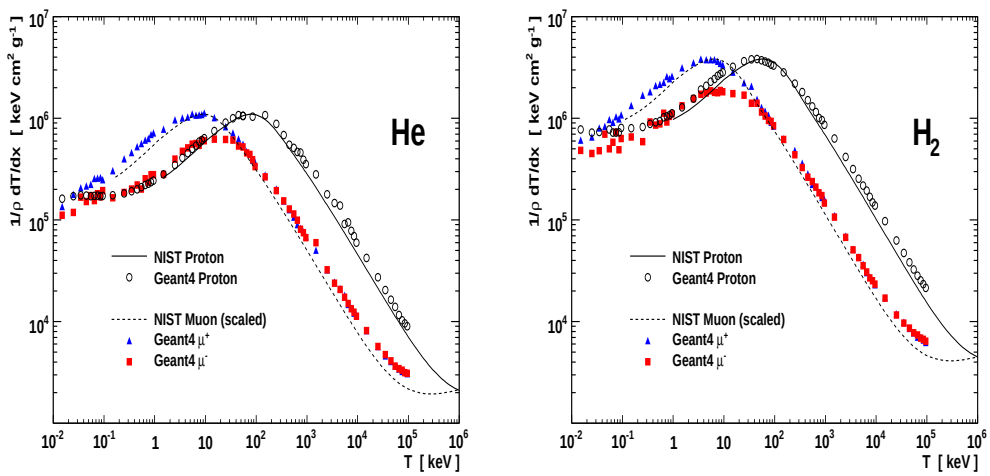

Figure 3.1: Comparison between experimental (NIST) and simulated (Geant4) stopping power for Helium (left) and Hydrogen (right).

A good agreement for positively charged muons and protons can be seen. Since these are positively charged particles they experience the processes of Muonium and Hydrogen formation (see section 3.3) in contrast to negatively charged muons. The cross-sections of these processes become significant for energies near and below the ionization peak. Therefore, negatively charged muons suffer less energy loss in this region than positively charged muons.

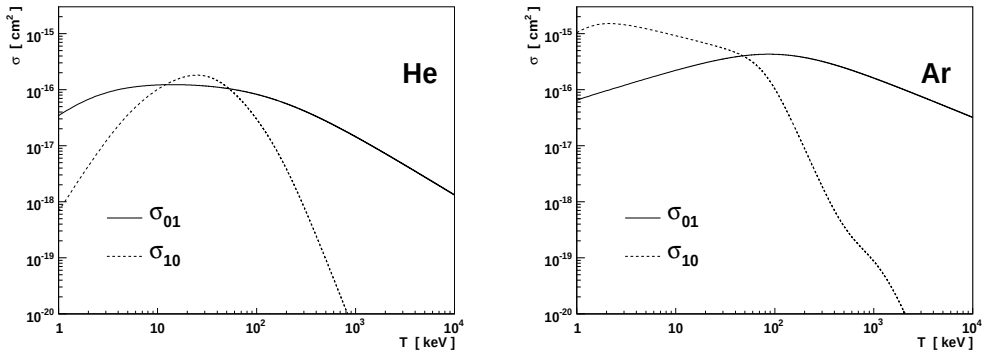

Figure 3.2: Muonium formation cross-section σ_{10} and Muonium ionization cross-section σ_{01} for μ^+ in Helium (left) and Argon (right).

Preferably, Helium is used as the retarding medium for μ^+ because the Muonium formation cross-section dominates over the electron stripping cross-section in all gases excluding Helium (see section 3.3). Furthermore, Helium has the highest ionization energy, of approximately 24.6 eV, of all materials which leads to fewer free electrons that could screen an electric field and fewer charge exchange processes. For μ^-, Hydrogen is used as the stopping medium because it has the smallest cross-section for muon capture by the medium atoms (see section 3.5).

3.3 Muonium and Hydrogen Formation

When positive particles travel through a medium they interact though charge exchange processes with the medium atoms. A μ^+ can capture an electron and become Muonium (Mu)

$$\mu^+ + \text{Atom} \rightarrow \text{Mu} + \text{Atom}^+ \tag{3.1}$$

whereas a proton can capture an electron and become Hydrogen (H)

$$\text{p} + \text{Atom} \rightarrow \text{H} + \text{Atom}^+ \tag{3.2}$$

where Mu and H are neutral bound states. The cross-section for electron capture is labeled as σ_{10} and that for ionizing the neutral bound state as σ_{01}. In principle, it is possible for a muon or for a proton to capture two electrons. However, it is not considered in the simulation because the cross-section of this process is several orders of magnitude smaller than single electron capture in Helium [20].

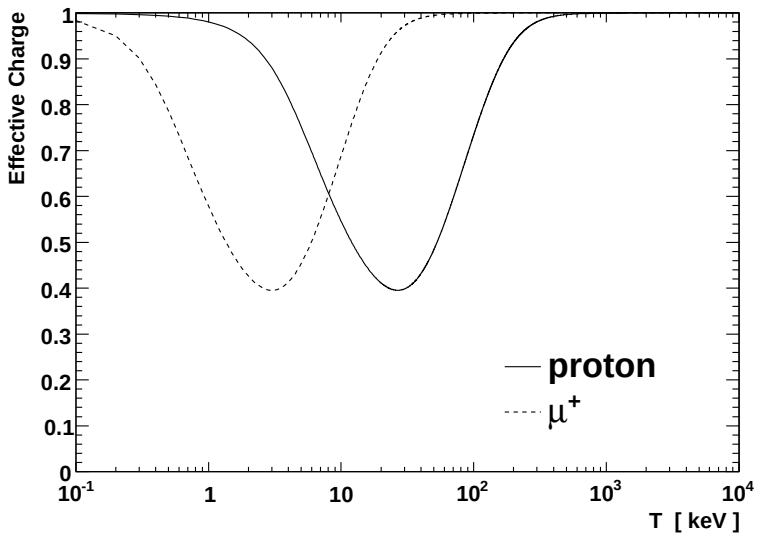

Figure 3.3: Effective charge for proton and μ^+ in Helium.

The cross-sections σ_{10} and σ_{01} for μ^+ in Helium, taken from [20], are shown in fig. 3.2. For reasons of comparison, the cross-sections in Argon are shown as well.

It can be seen that in Helium, except for the energy region around the ionization peak, the Muonium ionization cross-section σ_{01} strongly dominates over the Muonium formation cross-section σ_{10}. This is in contrast to all other gases. As an example the cross-sections in Argon are shown. This unique property of Helium leads to its usage as the stopping medium for μ^+. The resulting increased energy loss due to Muonium formation compared to μ^- is already implemented in Geant4 as shown fig. 3.1.

The superposition of σ_{10} and σ_{01} leads to the energy dependent effective charge approach

$$q_{\text{eff}}(T) = \frac{\sigma_{01}}{\sigma_{01} + \sigma_{10}} \tag{3.3}$$

with T the kinetic energy of μ^+ or proton respectively. Eq. (3.3) is implemented such that the applied Lorentz-Force is reduced linearly by the current value of q_{eff} where $0 < q_{\text{eff}} \leq 1$.

The minimum density, for which equilibrium energies according to eq. (2.4) are still expected, is $\rho_{\text{min}} = 1 \cdot 10^{-3}$ mg/cm^3. The minimum cross-section for μ^+ in Helium at which σ_{10} is larger than σ_{01} is approx. $\sigma_{\text{min}} = 1 \cdot 10^{-16}$ cm^2 (see fig. 3.2). This yields a maximum mean free path for the process of

Muonium formation

$$\lambda_{\mathrm{max,10}} = \frac{A}{\sigma_{\mathrm{min}} \cdot \rho_{\mathrm{min}}} \approx 0.5 \text{ mm} \tag{3.4}$$

where $A = 4.0026$u denotes the atomic weight of Helium. The value of $\lambda_{\mathrm{max,10}}$ is at least two orders of magnitude smaller than muons would travel in a typical cooling cell at energies below the ionization peak (see chapter 5). This leads to the validation of the effective charge approach from eq. (3.3) since $\lambda_{\mathrm{max,10}}$ is much smaller than the particles total path length. Therefore, instead of a discrete simulation of the processes of Hydrogen and Muonium formation, and the corresponding ionization processes, a continuous energy dependent Ansatz is sufficient that leads to an effective charge of μ^+ and proton.

The effective charge $q_{\mathrm{eff}}(T)$ for proton and μ^+ in Helium is shown in fig. 3.3. The cross-sections for μ^+ are again scaled from those for protons [20] via velocity scaling [10]. The effective charge has a large influence on the energy gain of the particles that have energies around the ionization peak. The Lorentz-Force from eq. (2.3) is greatly reduced up to approximately 60% in the region of Frictional Cooling. The effective electric field $\vec{E}_{\mathrm{eff}}$ as well as the effective magnetic field $\vec{B}_{\mathrm{eff}}$ scale linearly with q_{eff}

$$\vec{E}_{\mathrm{eff}}(\vec{x}) = q_{\mathrm{eff}} \cdot \vec{E}(\vec{x}) \tag{3.5}$$

$$\vec{B}_{\mathrm{eff}}(\vec{x}) = q_{\mathrm{eff}} \cdot \vec{B}(\vec{x}) \tag{3.6}$$

yielding the effective Lorentz-Force $\vec{F}_{\mathrm{L,eff}}$ that is used in the simulation

$$\vec{F}_{\mathrm{L,eff}}(\vec{x}) = q_{\mathrm{eff}}(T) \cdot \vec{F}_{\mathrm{L}}(\vec{x}) \tag{3.7}$$

3.4 Particle Decay

The decay of both positively and negatively charged muons is implemented in the simulation. In principle, the decay process can be applied on every particle. The proton is assumed to be stable since it has a mean lifetime much greater than the age of the universe.

The mean lifetime τ for each particle is taken from the Geant4 particle database. The current time in the proper system of the particle t_{p} is initialized to zero when the particle enters the cooling cell. During tracking, whether a particle decays is determined by the decay probability

$$p_{\mathrm{decay}} = 1 - \exp(-t_{\mathrm{p}}/\tau) \tag{3.8}$$

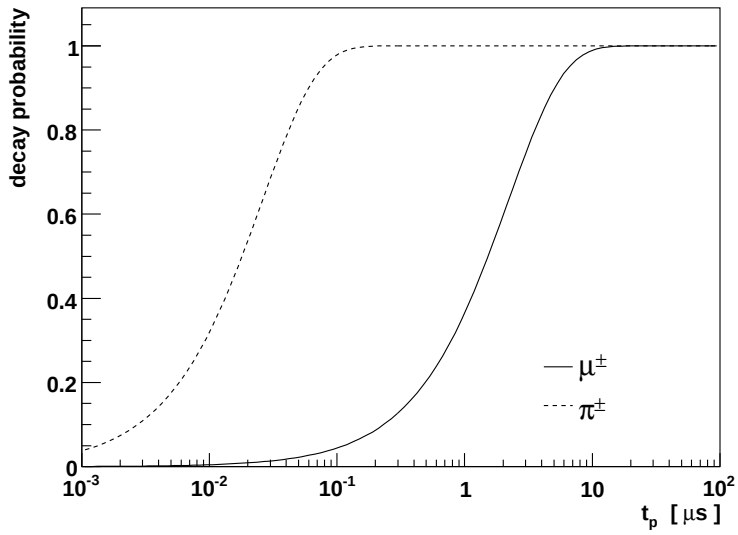

Figure 3.4: Decay probability plotted for $\mu^{\pm}$ and $\pi^{\pm}$

Muons have a mean lifetime of $\tau = 2.2$ μs and decay through the Weak Force according to

$$\mu^- \rightarrow e^- + \bar{\nu}_e + \nu_\mu \tag{3.9}$$

$$\mu^+ \rightarrow e^+ + \nu_e + \bar{\nu}_\mu \tag{3.10}$$

The equality of μ^+ and μ^- lifetimes has been established to be better than one part in 10^4 [21]. The corresponding decay probability is shown in fig. 3.4. For reasons of comparison the decay of charged π-mesons, which have a mean lifetime of $2.6 \cdot 10^{-2}$ μs, is also shown. Neither electrons nor positrons nor neutrinos are tracked or considered in the simulation. However, in the last chapter the number of free charges per muon track due to ionization is estimated.

3.5 Muon Capture

A negatively charged muon may be captured by a medium atom A into the orbit since the Coulomb interaction is attractive between nucleus and μ^-. The muon decays in the orbit of the atom (see previous section) end gets lost. The most likely process is

$$\mu^- + A \rightarrow A_\mu + e^- \tag{3.11}$$

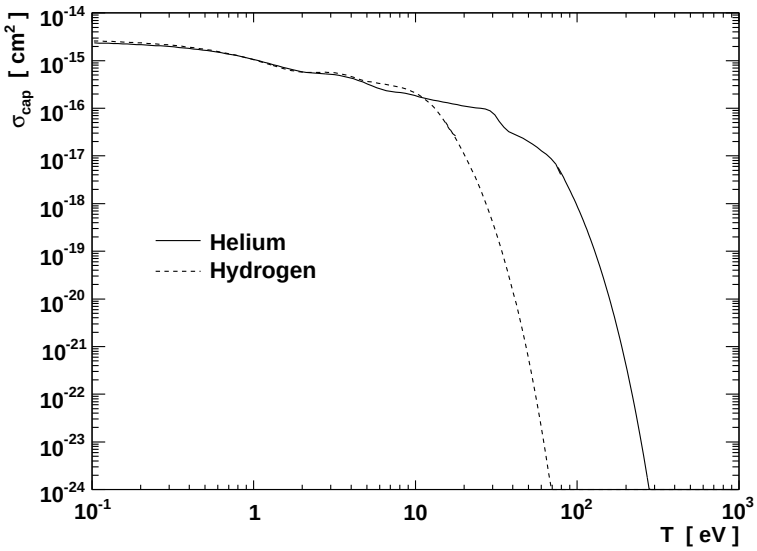

Figure 3.5: Capture cross-sections for μ^- in Helium and Hydrogen

where A_μ is an atom where an electron has been replaced by a μ^-. Only the capture into the orbits of atoms are considered in this work. Other processes, like the capture *into* the nucleus, have cross-sections in Hydrogen and Helium that are much smaller than those for the process mentioned above.

The cross-sections for μ^- capture into orbits of atoms in Helium and Hydrogen, taken from [22] and [23], are shown in fig. 3.5. The data points for each cross-section are interpolated via cubic splines and exponentially extrapolated to higher energies.

The cross-section for μ^- capture in Helium becomes significant below 200 eV whereas the cross-section in Hydrogen becomes significant only below approximately 60 eV. To maximize yield, we therefore use Hydrogen as the stopping medium for μ^-.

The capture cross-section σ_{cap} yields the energy dependent mean free path $\lambda_{\text{cap}}(T)$ for this process

$$\lambda_{\text{cap}}(T) = \frac{1}{n \cdot \sigma_{\text{cap}}} \tag{3.12}$$

where n denotes the density of atoms in the gas. Let Δl be the length the particle traveled between two steps, then the μ^- capture probability p_{cap} is

$$p_{\text{cap}} = 1 - \exp(-\Delta l/\lambda_{\text{cap}}(T)) \tag{3.13}$$

which was implemented in the simulation.

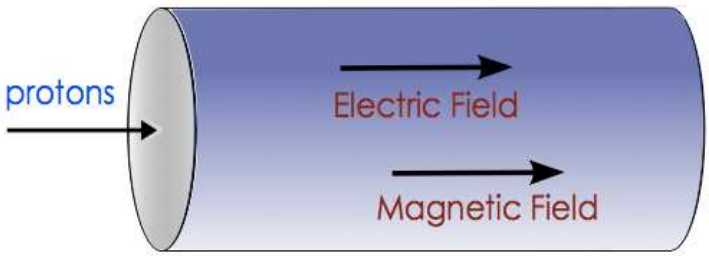

Figure 3.6: Setup of an exemplary gas cell

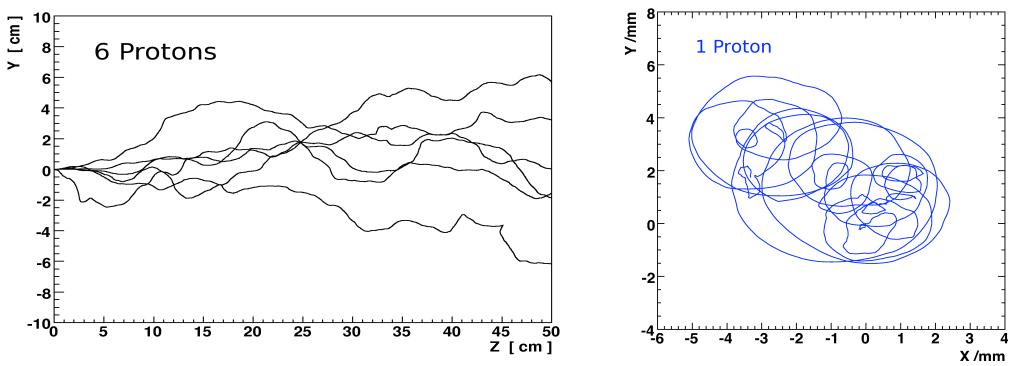

Figure 3.7: Typical trajectories of protons starting at 1 keV traversing through the gas cell. $E = 4$ kV/cm , $B = 1$ T.

3.6 Simulation of an exemplary Gas Cell

To validate the processes an exemplary cooling cell is simulated with Helium at a density of $\rho = 0.01$ mg/cm^3. The electric field E as well as the magnetic field B are aligned homogeneous along the z-axis. This will demonstrate how Frictional Cooling works and how the simulation results in principle must be interpreted.

The principle setup is shown in fig. 3.6. The gas cell consists of a tube with 50 cm in length and 20 cm in diameter. Protons enter the cell at the center with cartesian coordinates (0,0,0) and zero transverse momentum.

The trajectories of a few protons for typical settings of the field strengths are shown in fig. 3.7. Multiple scattering at nuclei and a resulting transverse spatial spread can be seen.

Fig. 3.8 shows the trajectories of some representative protons for three different strength of the magnetic field. The helical motion due to a magnetic

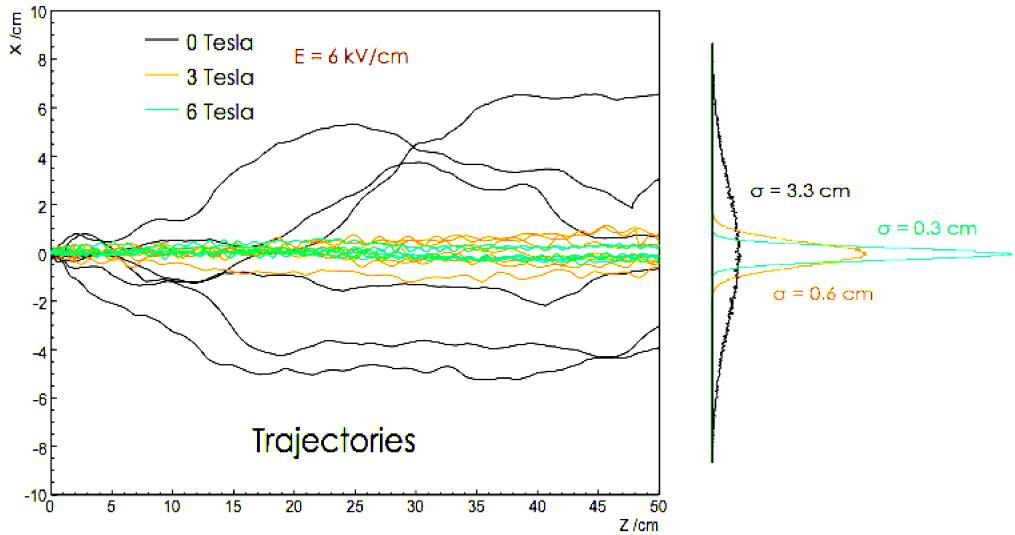

Figure 3.8: Trajectories (left) and spatial distributions at the end plane (right) of protons starting at 1 keV for three different strengths of the magnetic field and $E = 6$ kV/cm.

field can be seen clearly. Going from 0 Tesla to 3 Tesla leads to a strong collimation by approximately a factor of 5. This results in a significantly increased acceptance in a detector at the end plane of the cell.

The evolution of the kinetic energies of protons traversing through the gas at zero magnetic field is shown in fig. 3.9. It can be observed how protons reach an equilibrium energy T_{eq} independently from their starting energies.

The resulting energy spread in the energy distributions will always be a limiting factor in reducing beam emittances. It originates from the effect of scattering at nuclei.

The effective charge approach has a tremendous influence on the energy gain of particles near the ionization peak. Accelerating protons greater than approximately 10 keV does not yield much benefit since the necessary electric field strengths are nearly neutralized by charge exchange processes with the medium atoms (see fig. 3.3).

The small tail towards lower energies in the energy distributions originates from the fact that the cross-section for large angle displacement due to multiple scattering increases as the energy decreases (compare with fig. 2.1). If a proton has a negative z-component in momentum, it is first decelerated by the electric field until the z-component becomes positive again, then it is accelerated. Thus, large angle scatters yield a higher probability that protons

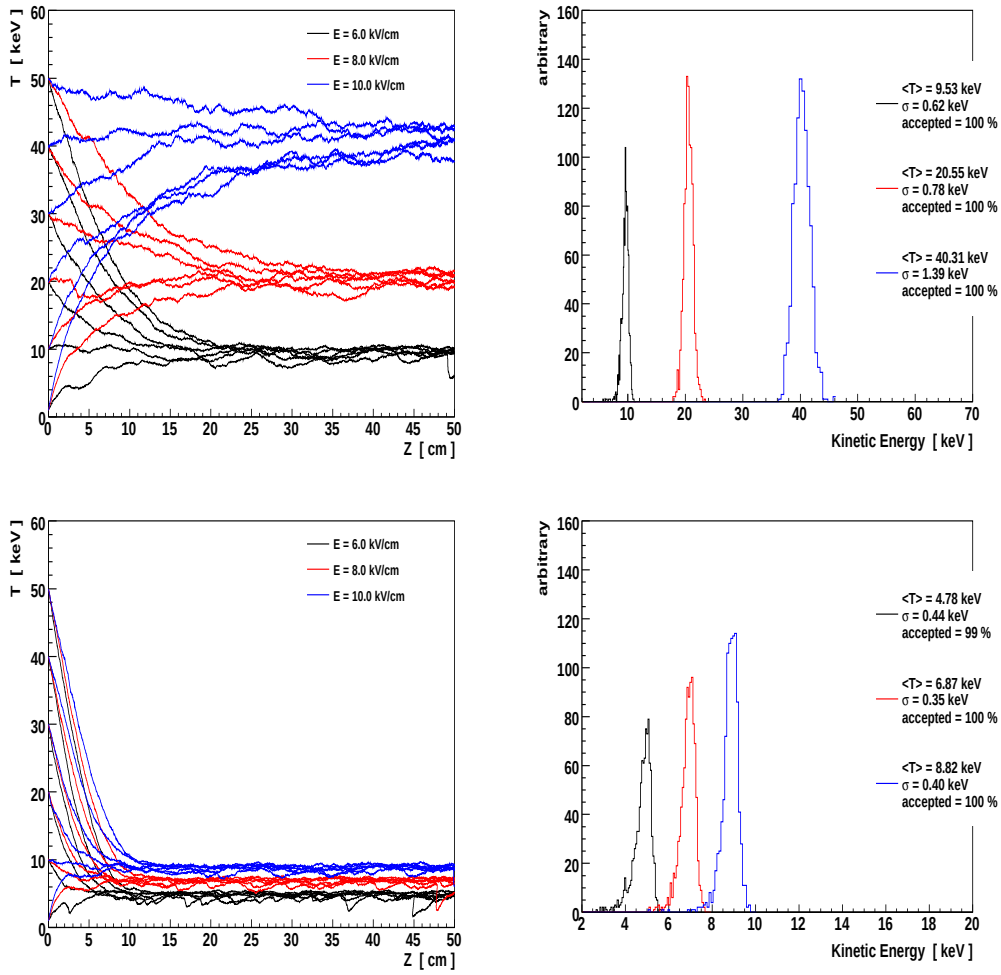

Figure 3.9: Kinetic energy versus z (left) for a few representative protons with starting energies from 1 to 50 keV for three different strengths of the electric field and zero magnetic field, and the corresponding energy distributions for 10^4 protons at the end plane (right) **without** (above) using the effective charge approach and **with** (below) using it. Accepted indicates the percentage of protons that reach the end plane.

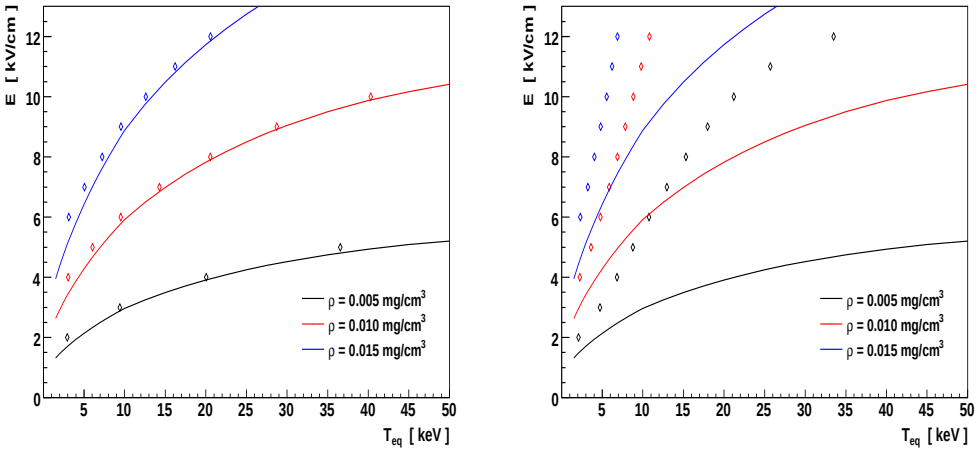

Figure 3.10: Applied electric field versus reached equilibrium energy **with** effective charge approach (right) and **without** (left) for three different densities at $B = 0$ T. Simulation results are shown as dots. For comparison, also the corresponding total stopping power taken from the NIST tables derived from setting $E = \frac{\mathrm{d}T}{\mathrm{d}x}$ is outlined.

are decelerated by the electric field.

In fig. 3.10, the applied electric field strength E versus the resulting equilibrium energy T_{eq}, as defined with the criteria from eq. (2.4), is shown for three different densities of the Helium gas. Simulation results and data for the stopping power in Helium, taken from the NIST tables, match very well if the effective charge approach is not used. Since the energy loss is simulated adequately, as presented in fig. 3.1, the simulated energy gain due to an electric field is also reasonably implemented. For comparison, a similar plot is shown on the right side of fig. 3.10 with using the effective charge approach. As expected, the same electric field strength leads to a strongly reduced equilibrium energy.

Applying a magnetic field only marginally reduces the resulting mean energies of the protons. However, a magnetic field results in a strong collimation and more surviving particles possessing lower energies. A reduction of only 1% in the average kinetic energy of a proton bunch at the end of the cooling cell was observed when a magnetic field of 3 Tesla is applied. A constant magnetic field does not change the kinetic energy of single particles in contrast to a magnetic field that varies with time.

Fig. 3.11 shows the movement of a single proton in vacuum in the x-y-

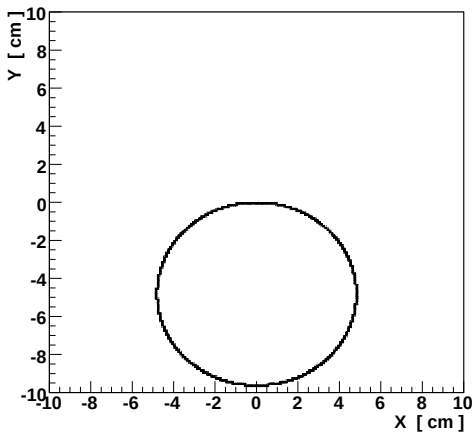

Figure 3.11: Movement of a single proton in vacuum at $B = 3$ T and $E = 0$ shown in the x-y-plane with an initial momentum direction vector of $(100, 0, 1)$ and a starting energy of 1 MeV.

plane. It has the initial momentum direction vector

$$\vec{P}_0 = (100, 0, 1) \tag{3.14}$$

at a starting energy of 1 MeV. The proton experiences a constant magnetic field of $B = 3$ T along the z-axis and zero electric field. Therefore, the cyclotron radius r_c is calculated as

$$r_\mathrm{c} = \frac{P_\mathrm{x}}{q \cdot B} = 4.814 \text{ cm} \tag{3.15}$$

which one obtains from the equality of the Lorentz and the centrifugal force. The simulated cyclotron radius is 4.813 cm, which is in very good agreement with the calculation. Thus, it can be assumed that the magnetic field B is also simulated accurately.

Chapter 4

Simulation of the FCD Experiment

In this chapter the Frictional Cooling demonstration (FCD) experiment with protons will be described. Electric and magnetic fields are discussed. The proton source is presented. Finally, the most important simulation results of the FCD experiment are given and interpreted.

4.1 Experimental Setup

The Frictional Cooling demonstration experiment consists of a gas cell filled with Helium at low densities, and placed in non-homogeneous electric and magnetic fields. The cell is a tube 10 cm in length and 3 cm in diameter. The gas cell construction including the accelerating grid that provides the electric field is shown in fig. 4.1. The proton source (see section 4.4) is variably mounted at the bottom of the cell. The accelerating grid consists of 21 metal rings which are connected in series by resistors. Up to 100 kV can be applied on the first ring which results in an electric field of approximately 10 kV/cm at maximum (fig. 4.3).

During the end stages of the experiment, the whole gas cell construction will be placed in a magnet (see fig. 4.5) to increase acceptance and to investigate the influence of a magnetic field on protons traversing through a gaseous medium. The magnet consists of a superconducting coil 18.2 cm in length and an inner radius of 5.6 cm (see fig. 4.6); it is able to provide up to 5 Tesla in its center. Fig. 4.2 shows a setup scheme of the final FCD experiment. The gas cell, shown in gray, is aligned parallel along the z-axis. At the end of the cell a silicon drift detector with an active circular area of 10 mm^2 measures the kinetic energy of the incoming protons.

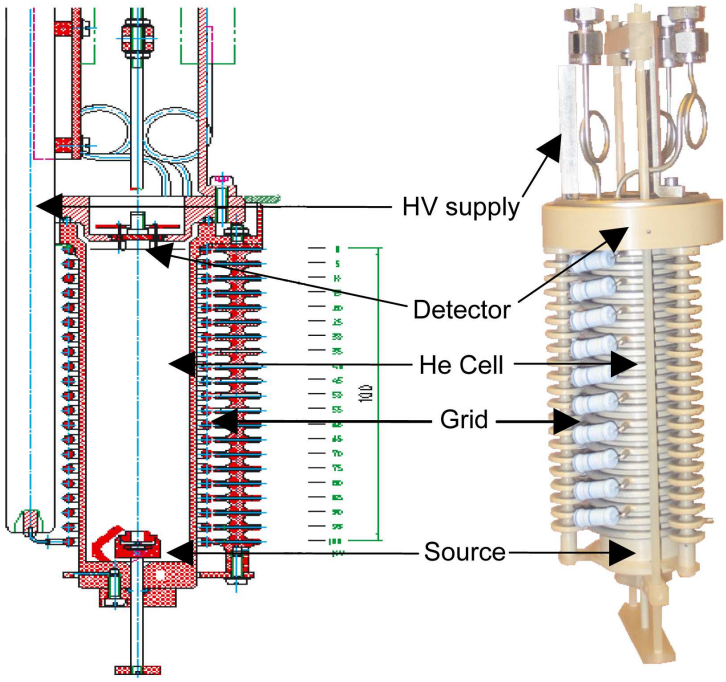

Figure 4.1: The gas cell construction including the accelerating grid.

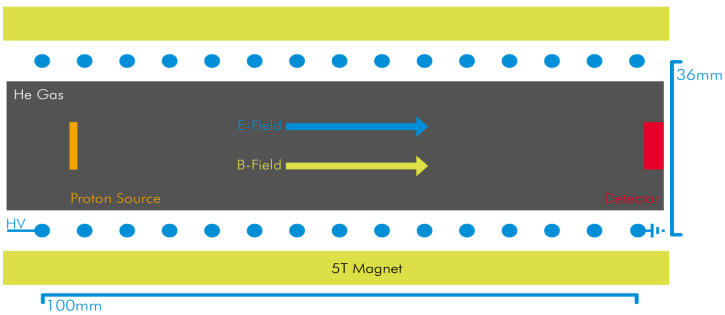

Figure 4.2: A schematical view of the FCD experiment.

4.2 Electric Field

A simulation of the electric potential setup by the accelerating grid was undertaken using SIMION 7.0 [24]. Fig. 4.3 shows the z-component of the electric field on the z-axis normalized to the high voltage HV that is applied on the first ring of the accelerating grid. The shape of the electric field does not depend on the value of HV. A large region from 3 to 9 cm is nearly

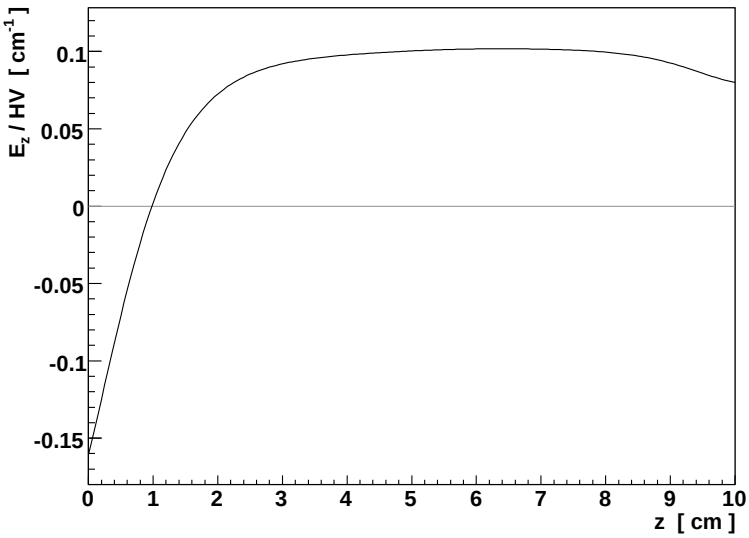

Figure 4.3: The z-component of the electric field on the z-axis in the FCD experiment normalized to the high voltage HV applied on the first ring of the accelerating grid.

homogeneous.

In order to make use of this field in the simulation, an interpolation between data points on a grid with fixed step size is required. Because of the geometry of the accelerating grid the field structure is symmetric around the z-axis. Therefore, the interpolation has to be done in two dimensions, namely in r and z. There are three important interpolation methods: Nearest neighbor, bilinear interpolation and bicubic interpolation [25] which originate from image processing. In the simulation, bilinear interpolation is used because it is an efficient compromise between accuracy and computation time. Nearest neighbor can be chosen as well to reduce computation time, but it is not recommended since the resulting accuracy is low.

In the following a short derivation is given and the algorithm applied on electric and magnetic fields. Assume that four amplitudes A_{ij} are given at the points (x_i, y_j) with $i, j = 1, 2$ and $a = |x_1 - x_2| = |y_1 - y_2|$ is the fixed step size of the grid. Suppose an amplitude $A(x, y)$ is in demand at the point (x, y), for $x_1 < x < x_2$ and $y_1 < y < y_2$.

The method of nearest neighbor is simply given as the amplitude A_{ij} whose coordinates x_i and y_j are closest to x and y.

For the method of bilinear interpolation three linear interpolations are

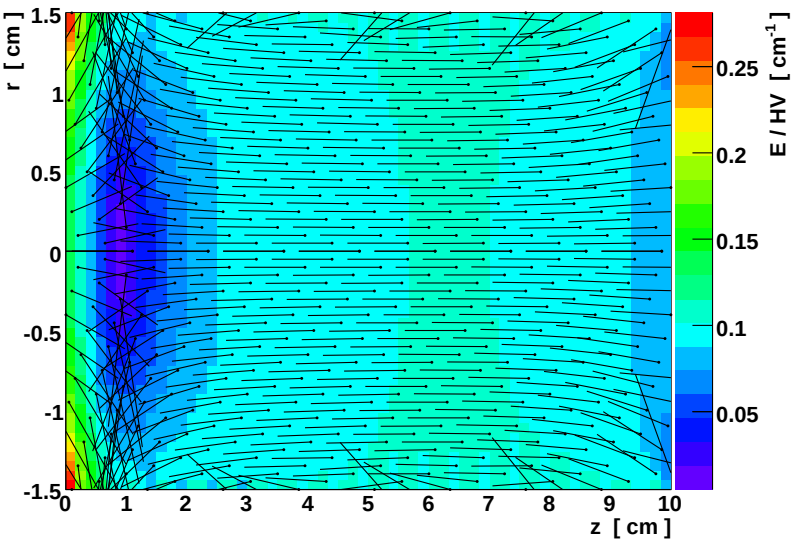

Figure 4.4: The magnitude of the electric field normalized by the high voltage HV applied on the first ring, with electric field vectors plotted on top, calculated with the bilinear interpolation algorithm.

required to obtain $A(x, y)$:

1. linear interpolation between A_{11} and A_{21} with result defined as B_1
2. linear interpolation between A_{12} and A_{22} with result defined as B_2
3. linear interpolation between B_1 and B_2.

The last interpolation yields $A(x, y)$ which can therefore be expressed as

$$\begin{aligned} A(x,y) = \{ \ (x_2 - x)(y_2 - y) \cdot A_{11} \ &+ \ (x - x_1)(y_2 - y) \cdot A_{21} + \\ (x_2 - x)(y - y_1) \cdot A_{12} \ &+ \ (x - x_1)(y - y_1) \cdot A_{22} \ \}/a^2 \end{aligned} \quad (4.1)$$

Using bilinear interpolation from eq. (4.1) a reasonable representation of the electric field is reached. The resulting field is displayed in fig. 4.4.

4.3 Magnetic Field

For use in the cooling simulation, the magnetic field of the FCD experiment was calculated using the law of Biot-Savart [26] that holds

$$d\vec{B} = \frac{\mu_0}{4\pi} \frac{I d\vec{l} \times \vec{r}}{r^3} \quad (4.2)$$

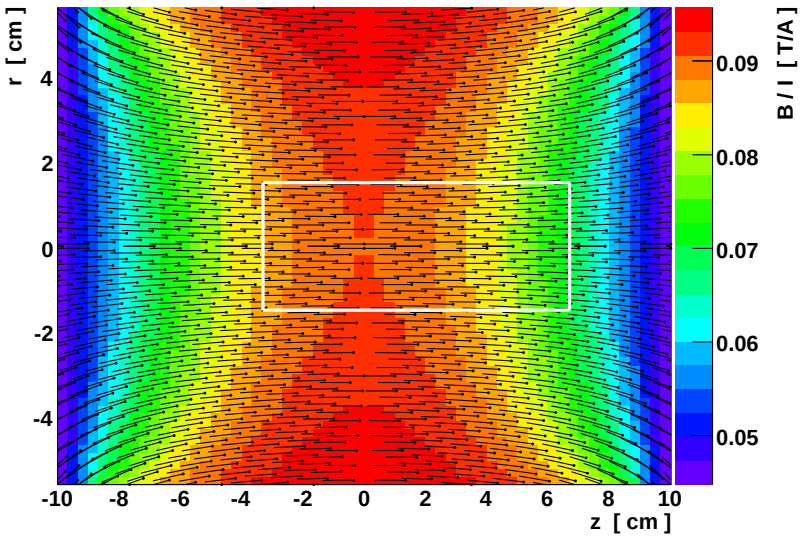

Figure 4.5: The magnitude of the magnetic field normalized to the coil current I with The magnetic field vectors plotted on top. The white lines represent the gas cell location.

where I denotes the current through the superconducting coil; $\mathrm{d}\vec{l}$ a vector, with a magnitude equal to the length of the differential element of the wire and pointing along the current; $d\vec{B}$ is the differential contribution to the magnetic field resulting from $\mathrm{d}\vec{l}$; μ_0 is the permeability of free space, equal to $4\pi \cdot 10^{-7}$ Tm/A; and $\vec{r}$ the displacement vector in the direction pointing from the wire element towards the point at which the field is computed.

Using this equation, the magnetic field for one current-loop is calculated. The entire magnetic field is then the sum of the magnetic fields of all current-loops in the magnet core. The resulting total magnetic field strength normalized by I and interpolated using eq. (4.1) is shown in fig. 4.5. The corresponding field vectors are plotted as well. The white lines represent the borders of the gas cell. The indicated position of the cell is the most probable given experimental construction requirements. As shown in fig. 4.5, the gas cell begins at a channel offset O_{chan} respective to the leading edge of the magnet of

$$O_{\mathrm{chan}} = 6.7 \text{ cm} \tag{4.3}$$

Fig. 4.6 shows a schematic drawing of the superconducting magnet and the resulting z-component of the magnetic field normalized to I on the z-axis. The field structure is far from homogeneous. However, to collimate strongly

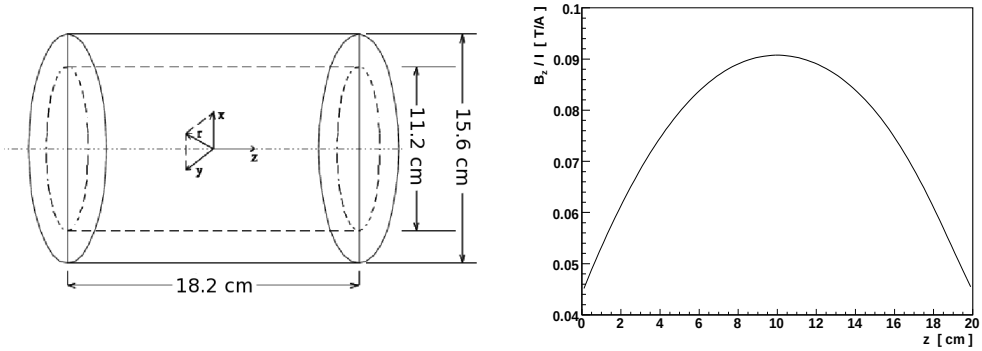

Figure 4.6: A schematic drawing of the magnet (left) and the z-component of the magnetic field on the z-axis normalized to I (right).

in order to maximize yield the proton source will be placed in regions of high magnetic field strengths.

4.4 Proton Source

The proton source of the FCD experiment consists of a radioactive layer of Americium-241 (Am241) that continuously emits α particles. These particles hit a Mylar foil with a thickness adjustable from 12 to 36 μm. The α particles penetrate through the Mylar and eventually break the bonds between the Carbon and Hydrogen atoms. Near the surface of the foil the protons (H^+) can escape with thermal energies. After their release from the Mylar foil, they are immediately accelerated by the electric field. Fig. 4.7 shows a scheme of the proton source. A detailed simulation of the proton source was undertaken in [27] where also a more detailed description of the mechanisms can be found.

A simulation of the proton source yielded a spatial distribution of the exit point for a proton emerging from the foil. Fig. 4.7 shows the probability density depending on radius and thickness of the Mylar foil that is implemented in the simulation.

In order to maximize the yield in the detector it is favorable to get more protons out of the center of the source since the accelerating electric field is highest on axis. Therefore, using foil thicknesses between 28 and 30 μm is recommended, as can be seen in fig. 4.8. Furthermore, the proton source should be placed in regions of high electric field strength. For this purpose, the source offset, that indicates the distance between the beginning of the gas cell and the source, O_{sour}, will be at least 2 cm (see also fig. 4.3).

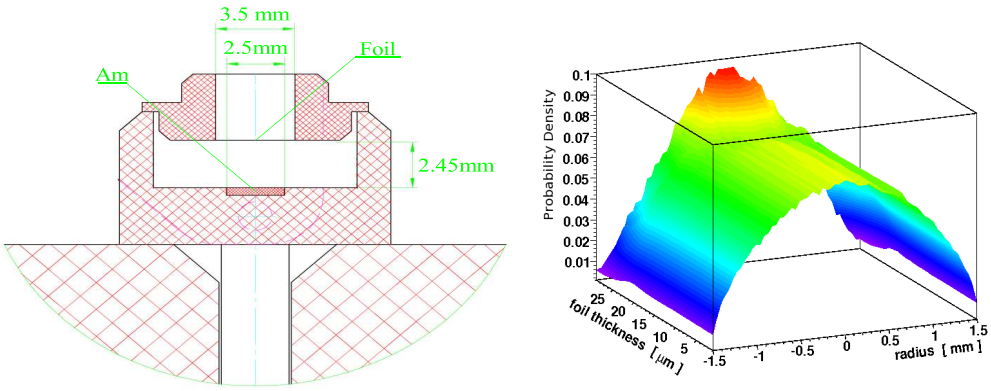

Figure 4.7: Left: Scheme of the proton source of the FCD experiment. Right: Probability density for protons exiting the foil as a function of radius and foil thickness.

4.5 Simulation Results

4.5.1 Conditions

Fig. 4.9 shows the principle setup used in the simulation. The gas cell, visible in gray, is placed inside the magnet with $O_{\text{chan}} = 6.7$ cm. The source construction consists of a source holder made out of plastic which can be moved back and forth along the z-axis. Additionally, a source delimiter 4 mm in length is placed on top of the holder which, in the experiment, keeps the Mylar foil in position. The delimiter reduces the proton rate by approximately 30 % because protons are absorbed by the plastic. In experiment and simulation the Mylar foil, 3.4 mm in diameter, is positioned between holder and delimiter. At the end of the gas cell, a detector, 3.2 mm in diameter, measures the kinetic energy of the incoming protons.

In the simulation, protons leave the source with a kinetic energy of 22 eV and a momentum direction of (0,0,1). This is at least two orders of magnitude below the final energies after acceleration. Compared to thermal energies (see section 4.4), this is a good approximation of the experimental situation. Energies below approximately 20 eV can not be assigned initially in Geant4, or the particles will not be tracked.

The Mylar foil is radially centered inside the gas cell at $O_{\text{sour}} = 2.5$ cm. The simulated spatial distribution of protons at the source is that of fig. 4.8 with a thickness of 23 μm for the Mylar foil. A gas cell filled with Helium at a density of 0.01 mg/cm^3 is simulated, corresponding to a pressure of 58.2 mbar at a temperature of 290 K.

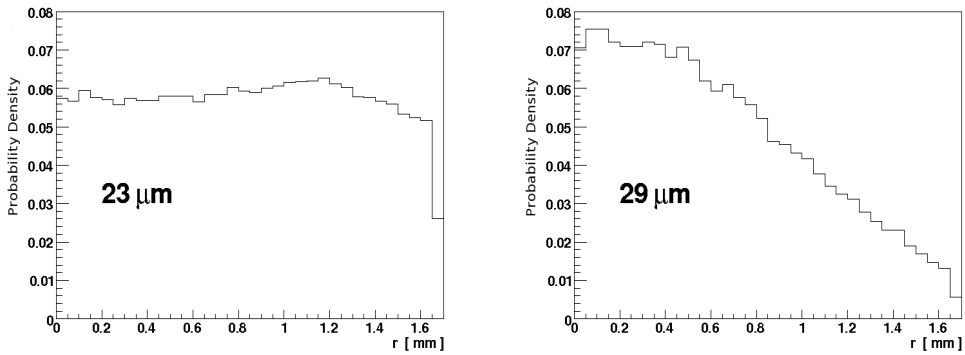

Figure 4.8: Probability density of protons exiting the foil as a function of radius for 23 μm (left) and 29 μm (right) thickness of the Mylar foil.

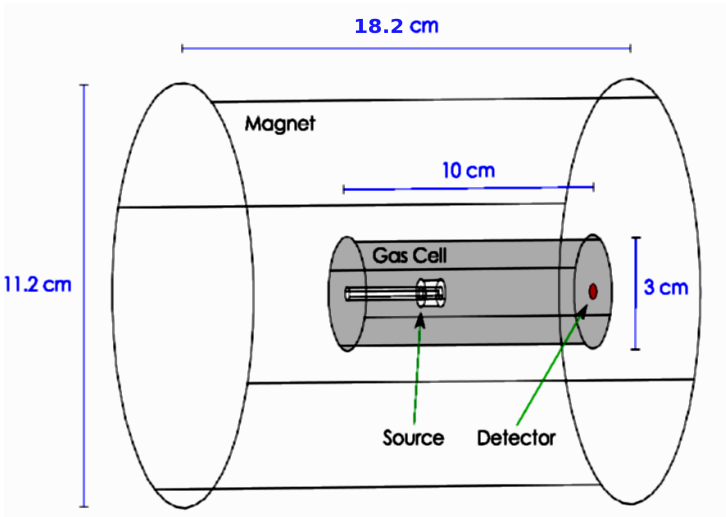

Figure 4.9: Principle setup used in the simulation of the FCD experiment.

If not mentioned otherwise, all results presented were achieved with the conditions above. The effective charge approach as shown in eq. 3.3 was always used.

4.5.2 Kinetic Energy

Fig. 4.10 shows the evolution of the kinetic energies of protons as well as the corresponding energy distributions at the end plane. The mean kinetic energy

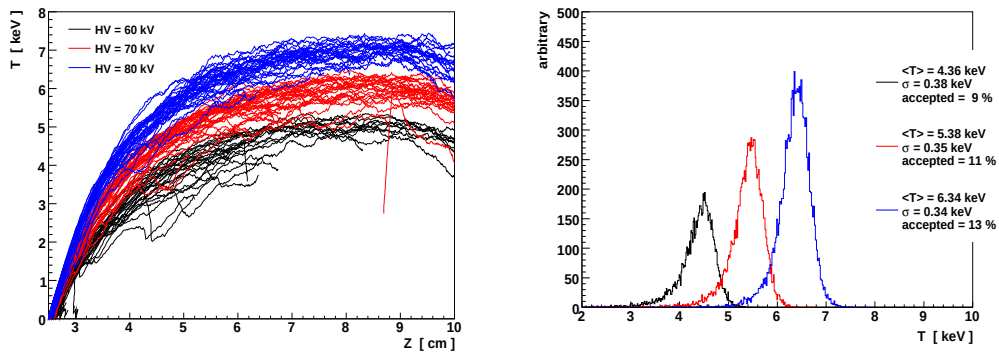

Figure 4.10: Kinetic energy versus z (left) for a few representative protons and the corresponding energy distributions for 10^4 protons at the end plane (right), for three different strength of the electric field and $I = 10$ A. A fairly large number of protons reaches the end plane of the cell (accepted).

of the protons at the end of the cell increases with electric field strength. The kinks in the left plot represent sudden large losses of energy due to large angle scatters at nuclei. If this angle is larger than $\pi/2$ then the protons get decelerated by the electric field and reaccelerated.

The cross-section for large angle scatters increases with decreasing kinetic energy of the particles and with increasing density of the gas. Therefore, the tail towards lower energies in the energy distributions increases with decreasing electric field strength. Also, the number of protons reaching the end plane of the cell significantly increases with rising electric field.

Fig. 4.11 shows the high voltage HV and the density ρ versus the mean kinetic energy of the protons at the detector. The applied electric field has an almost linear dependence of the kinetic energy, whereas the density has an exponential behavior. In the following, this behavior is described more quantitatively.

The change in kinetic energy $\mathrm{d}T$ along a path segment $\mathrm{d}\vec{x}$ holds

$$\frac{\mathrm{d}T}{\mathrm{d}\vec{x}}\hat{v} = \vec{F}_{\mathrm{L,eff}}(\vec{x}) - f_{\mathrm{stop}}(T)\hat{v} \tag{4.4}$$

where $\vec{F}_{\mathrm{L,eff}}(\vec{x})$ denotes the effective Lorentz-Force from eq. (3.7) and $f_{\mathrm{stop}}(T)$ the total stopping power taken from the NIST tables (fig. 2.1).

For this simple approach it is assumed that protons do not undergo any lateral displacement. This Ansatz is justified since the total path of protons that make it to the detector (fig. 4.12) is not much larger than the minimum

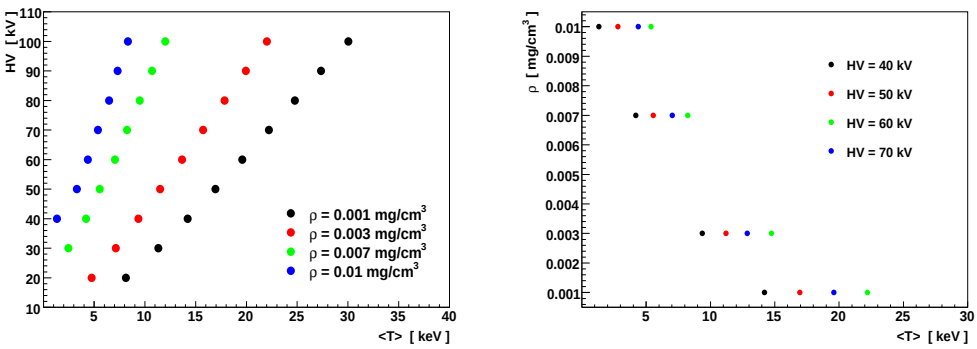

Figure 4.11: Simulation results: high voltage HV (left) and density ρ (right) versus mean energy for $I = 0$.

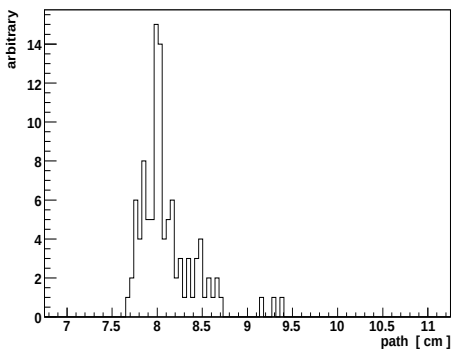

Figure 4.12: Total path length of protons that make it to the detector, at $HV = 70$ kV and zero magnetic field.

path of 7.5 cm for typical conditions. Without radial velocity components $\vec{v} \times \vec{B} = 0$ everywhere so eq. (4.4) simplifies to

$$\frac{\mathrm{d}T}{\mathrm{d}\vec{x}}\hat{v} = \vec{E}(\vec{x}) \cdot q_{\mathrm{eff}}(T) - f_{\mathrm{stop}}(T)\hat{v} \tag{4.5}$$

where $q_{\mathrm{eff}}(T)$ is the effective charge from eq. (3.3).

For the energy gain it is assumed that the radial component of the electric field is zero (fig. 4.4). Furthermore, $E_z(\vec{x})$ is assumed to be constant in the radial direction. Taking these simplifications into account, eq. 4.5 yields the continuous loss approximation

$$\frac{\mathrm{d}T}{\mathrm{d}z} = E_z(z) \cdot q_{\mathrm{eff}}(T) - f_{\mathrm{stop}}(T) \tag{4.6}$$

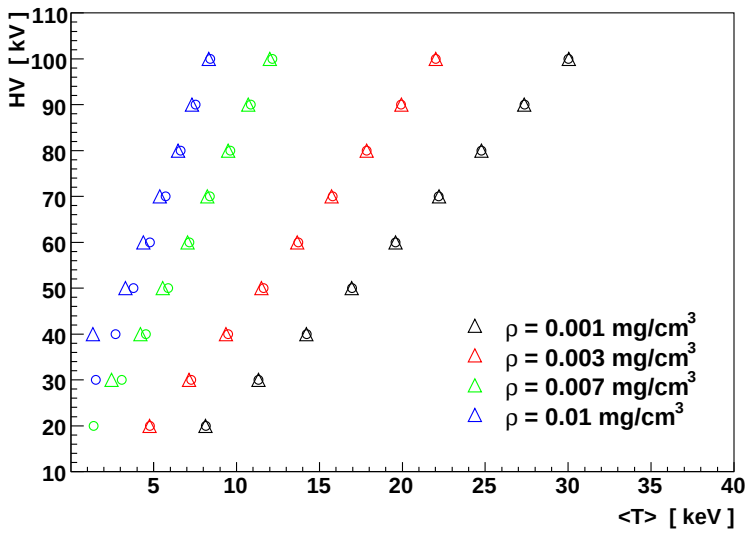

Figure 4.13: High voltage HV versus mean energy in the detector at $I = 0$. Simulation results (triangles) and continuous loss approximation (circles) are compared.

where $E_z(z)$ is shown in fig. 4.3.

Eq. (4.6) is a first order differential equation of the form $\mathrm{d}y/\mathrm{d}x = f(x, y)$ that is numerically solved by a 4th-order Runge-Kutta-Method. This was done and compared with the simulation as shown in fig. 4.13. Data from the simulation are shown as triangles whereas circles represent values calculated with the continuous loss approximation. This naive model matches the data from the simulation rather well. At the lower mean energies, differences become visible. These appear due to effects of multiple scattering, which increase with increasing density and decreasing kinetic energy.

Without multiple scattering, simulation results and the continuous loss approximation from eq. (4.6) match exactly. This shows once more that energy loss processes are implemented well in Geant4 and that the interpolation of the electric field was done sufficiently accurately.

Fig. 4.14 shows results of a simulation run without any lateral displacement due to multiple scattering. Multiple scattering has three major effects: the reduced energy gain due to an electric field, the appearance of a tail towards lower energies in the energy distribution and a significantly reduced acceptance in a detector at the end of the cell.

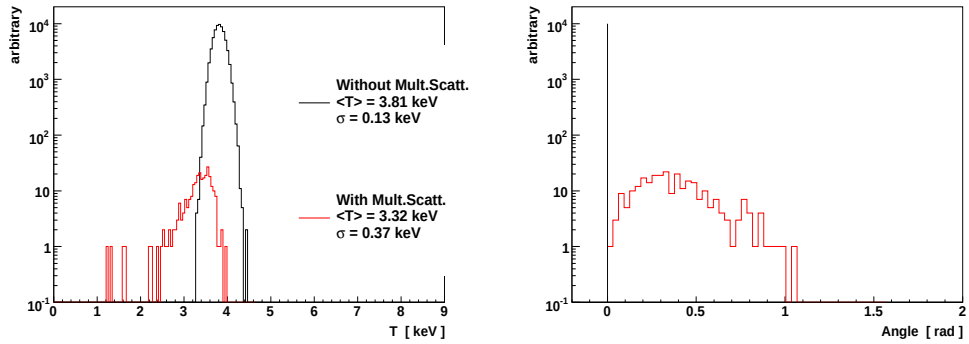

Figure 4.14: Left: energy distributions at the end plane for 10^4 protons for $HV = 50$ kV and $I = 0$. For the red curve multiple scattering is turned on in the simulation, for the black one it is turned off. Right: the corresponding angular distributions in radiants respective to the z-axis at the detector.

4.5.3 Acceptance in the Detector

The acceptance in the detector A_{D} at the end of the gas cell is defined as

$$A_{\mathrm{D}} = n_{\mathrm{D}}/N \tag{4.7}$$

where N denotes the total number of particles entering the cooling section and n_{D} the number of particles that make it to the detector. In order to maximize data-taking rates in the experiment, it is favorable to increase A_{D}. To reach higher values of A_{D} several approaches can be made.

A first idea is to put the gas cell construction in a magnetic field to collimate the particles. Fig. 4.15 shows that this is promising. The number of protons that make it to the end plane increases strongly with increasing strength of the magnetic field. A current of 50 A through the coils of the magnet is not favorable because the collimation towards the center of the cell is reduced. The protons are concentrated towards a ring of approximately 0.5 cm due to the radial component of the magnetic field (see fig. 4.5).

Another approach can be seen in fig. 4.16. The gas cell is placed into the magnet. The Channel offset O_{chan} as well as the source offset O_{sour} are varied. A_D increases significantly when O_{sour} increases and O_{chan} decrease. The black dot indicates the conditions for the previously presented simulation runs. The higher the source offset the less the path the protons travel to reach the detector and the higher the electric field strength. The acceptance rises with decreasing channel offset because the last centimeters until protons reach the

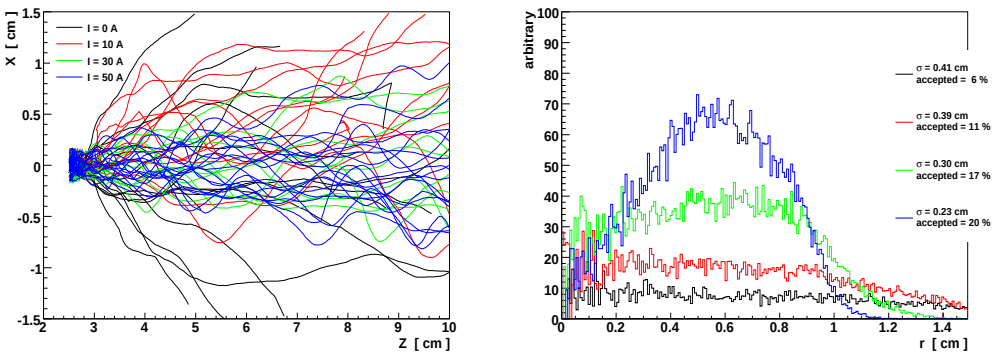

Figure 4.15: Trajectories of protons (left) traversing through the cell for four different strengths of the magnetic field at $HV = 70$ kV and the corresponding spatial distributions at the end plane (right). A fairly large number of protons reaches the end plane of the cell (accepted).

detector are then in regions of high magnetic field strengths which leads to higher collimations.

Fig. 4.17 shows high voltage HV versus acceptance A_D in the detector. Electric field strengths significantly increase the acceptance in the detector. Also a decrease of the density of the Helium gas is favorable, since the mean free path between scatterings scales as $1/n$ where n denotes the density of atoms in the gas.

The thickness of the Mylar foil of the proton source may also be varied. This is shown in fig. 4.18. A_D increases by approximately a factor of two when using foil thicknesses around 29 μm which is not significant. The mean energy at the detector does not seem to depend on the thickness of the Mylar foil. The differences appear due to statistical fluctuations.

In summary, in order to obtain a high acceptance in the detector, it is favorable to increase the electric field strength and lower the density. High thicknesses of the Mylar foil should be used that provide high proton production rates.

Furthermore, when the magnetic field collimates protons, a central field strength of around 2.5 T, which is reached at 30 A coil current, is optimal. The construction constraints should be overcome to be able to lower the channel offset, in order to increase the data rate. An increase in the source offset is favorable but at the same time protons travel a smaller path until they reach the detector. Therefore, reaching an equilibrium energy would become less likely (see also fig. 4.20).

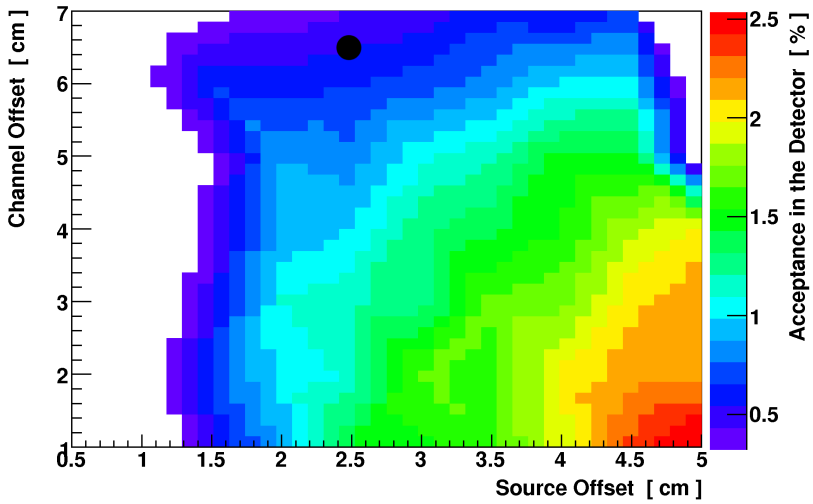

Figure 4.16: Channel offset versus source offset at $HV = 70$ kV and $I = 30$ A. The color palette represents the resulting acceptance A_D in the detector. The black dot indicates the conditions for the previously presented simulation runs.

Simulations with 10^4 protons were undertaken to determine the maximum acceptance achievable in the Frictional Cooling demonstration experiment. A configuration that leads to a high acceptance is:

- High voltage: 80 kV ($\sim$ 8 kV/cm at maximum)
- Density: 0.001 mg/cm^3
- Coil current: 30 A ($\sim$ 2.5 T at maximum)
- Foil thickness: 29 μm
- Source offset: 4 cm
- Channel offset: 1 cm

This setup yields $A_\mathrm{D} = 13.2$ %. Therefore, for a source with a proton production rate of 1 kHz a data-taking rate of approx. $5 \cdot 10^5$ protons per hour is expected, which corresponds to a good amount of data on a reasonable timescale.

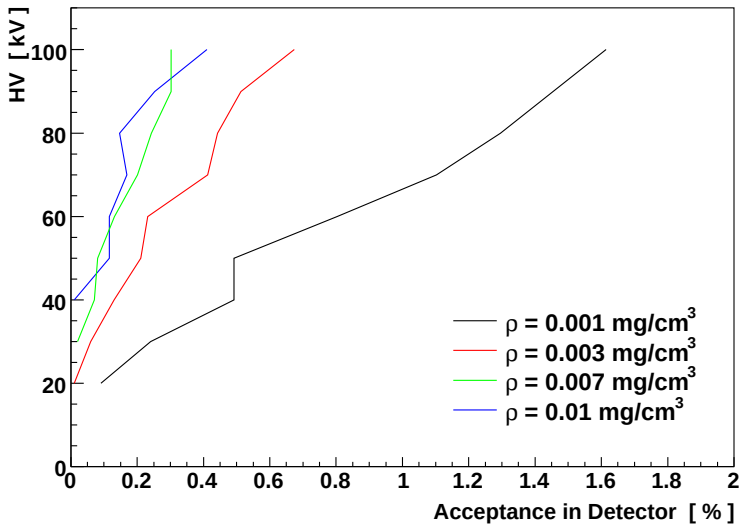

Figure 4.17: High voltage HV applied on the first ring versus the acceptance A_{D} in the detector for four densities at $I = 0$.

The foil is held by a delimiter made out of plastic, 4 mm in length, that stops a large amount of protons within the first millimeters. If the experiment could be run without it, the acceptance would significantly increase. A simulation run under the configuration above without this delimiter was done and led to $A_{\mathrm{D}} = 18.5$ % meaning that the proton rate would strongly increase by approximately 30 %. Therefore, it is recommended to run the experiment without the delimiter.

4.5.4 Equilibrium Energy

In order to fully demonstrate the principle of Frictional Cooling it is necessary to make use of sources that provide protons with different initial energies. If protons entering the cooling section at different energies T_0 end up at the same average kinetic energy then the principle of Frictional Cooling is empirically demonstrated.

Fig. 4.19 shows energy distributions of protons that enter the cooling cell with a Gaussian distribution in energy at a mean of T_0 and a standard deviation σ_0. Simulation runs at 70 kV high voltage and zero magnetic field were performed. Regardless of their starting energy, the proton bunches reach an equilibrium energy of 5.5 keV in the detector. This can already be

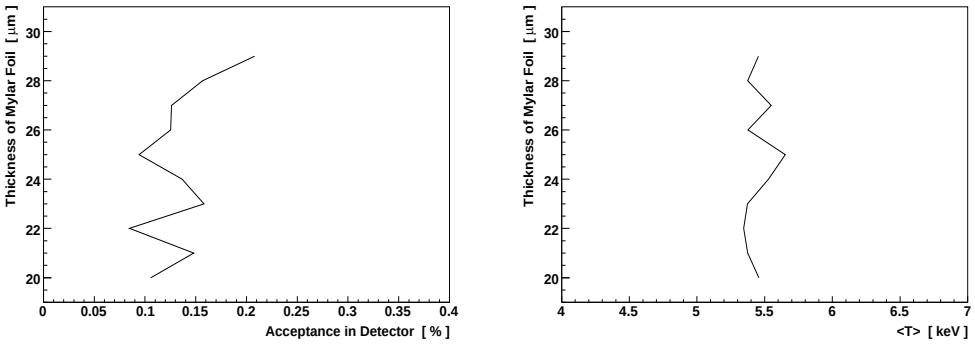

Figure 4.18: Acceptance (left) and average kinetic energy (right) in the detector at $HV = 70$ kV and $I = 0$ for various thicknesses of the Mylar foil.

described as the cooling of proton bunches since reducing the total energy spread leads to a reduction of the total momentum. In particular, the right plot of fig. 4.19 shows the energy distributions with the same conditions but at a coil current of $I = 30$ A. The resulting magnetic field leads to more surviving protons at lower energies which decreases the equilibrium energy slightly.

In order to show that the mean energy of the protons is an equilibrium energy, according to eq. (2.4), it is required that

$$\frac{\mathrm{d}T_{\mathrm{bunch}}}{\mathrm{d}z} = 0 \tag{4.8}$$

holds for a z along the gas cell, where $\mathrm{d}T_{\mathrm{bunch}}$ denotes the average change in energy for a bunch of protons. This is done by applying the previously mentioned continuous loss approximation.

Fig. 4.20 shows the result for a density of the Helium gas of 0.01 mg/cm^3 and a high voltage of $HV = 70$ kV. Since the criteria from eq. (4.8) holds, the protons end up in the same equilibrium energy. The energy variation along z becomes smaller than 0 to the end of the cell. This is due to a decreasing electric field strength in this region (see fig. 4.3).

The right plot of fig. 4.20 shows $\mathrm{d}T/\mathrm{d}z$ as a function of z for different densities and a starting energy of 0.1 keV. Lower densities do not lead to equilibrium energies since the criteria from eq. (4.8) is not met. The energy loss due to the gaseous medium is too weak and cannot oppose the electric field introduced by a high voltage of 70 kV within the dimensions of the FCD experiment. Therefore, in order to still use lower densities lower electric field strengths must be applied to reach equilibrium energies.

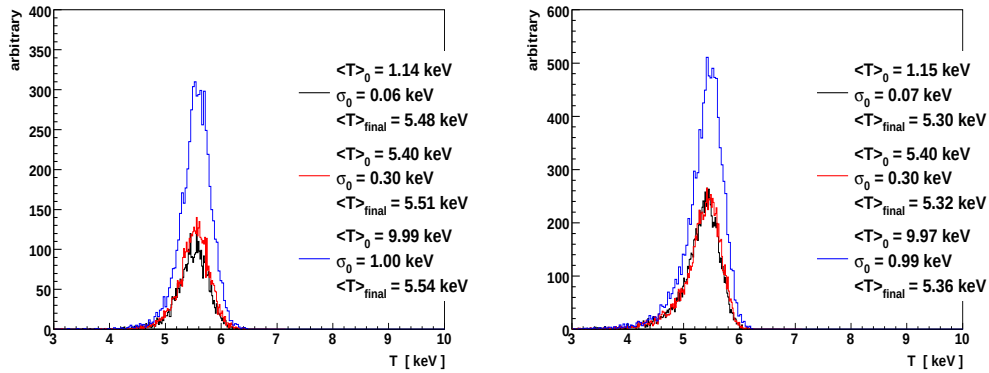

Figure 4.19: Energy distributions of 10^4 protons for $HV = 70$ kV at the end plane of the gas cell for different starting energies T_0 and $I = 0$ (left) and $I = 30$ A (right).

Fig. 4.21 shows the minimum distance z_{eq} along the z-axis required to reach equilibrium energy as a function of high voltage and density of the gas. A large region is available to demonstrate the principle of Frictional Cooling. Higher densities are favorable since protons reach an equilibrium earlier in z. However, the energy spread due to multiple scattering increases. A good compromise are densities of the Helium gas around 0.01 mg/cm^3.

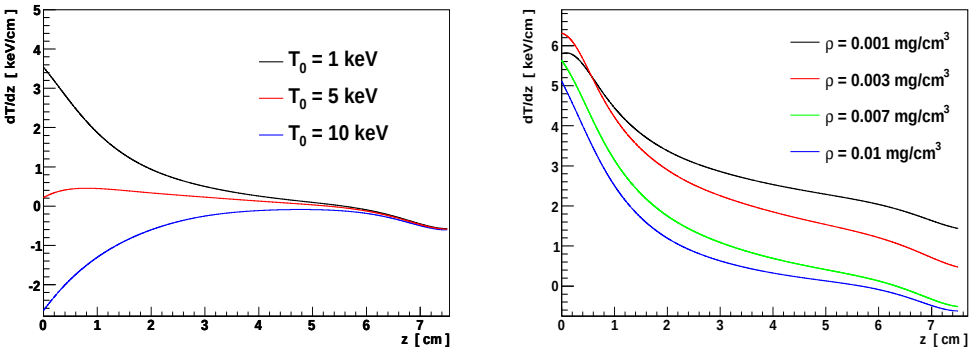

Figure 4.20: Development of $\mathrm{d}T/\mathrm{d}z$ calculated with the continuous loss approximation with $HV = 70$ kV and $I = 0$ for three different starting energies (left) at 0.01 mg/cm^3, and for different densities (right) at $T_0 = 0.1$ keV.

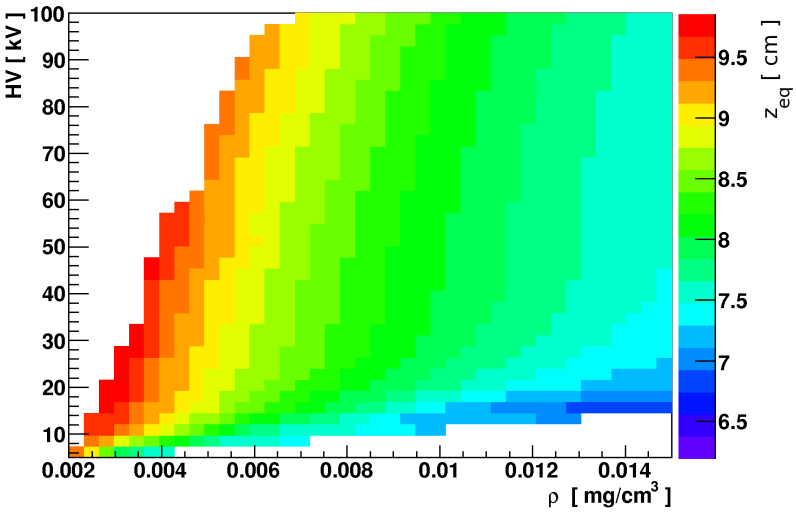

Figure 4.21: Minimum distance z_{eq} along the z-axis required to reach equilibrium energy as a function of high voltage HV and density ρ of the gas.

Chapter 5

Simulation of a Muon Cooling Channel

In this chapter an outline of a possible Muon Collider is given which makes use of the concept of Frictional Cooling. The geometry of the cooling channel as well as its electromagnetic fields are introduced. First simulation results are presented and interpreted. Emittance and luminosity of a muon beam in a Muon Collider are calculated.

5.1 Outline of a Muon Collider Scheme

In the very beginning of every collider the particles that physicists want to collide need to be produced. For a Muon Collider this will be realized by bombarding a target (e.g. Copper, Carbon) with protons produced by a MW accelerator (fig. 5.1). Due to the nuclear interactions, pions are produced that are captured and collimated in the pion decay channel with strong magnetic fields of up to 20 T. In this region, they decay weakly according to

$$\pi^- \rightarrow \mu^- + \bar{\nu}_\mu \tag{5.1}$$

$$\pi^+ \rightarrow \mu^+ + \nu_\mu \tag{5.2}$$

with a mean lifetime of $\tau = 26$ ns (see fig. 3.4). After several tens of ns of drift, muons with a large momentum spread enter the main cooling section, the muon cooling channel. Here, the emittance of the muon bunch must be reduced by several orders of magnitude. Muons with lower momenta are already cooled and extracted when they first penetrate through the channel; those with higher momenta travel all the way through and reach the phase rotation section located in vacuum. Here, muons are reflected which then again travel through the cell where they get eventually cooled and extracted.

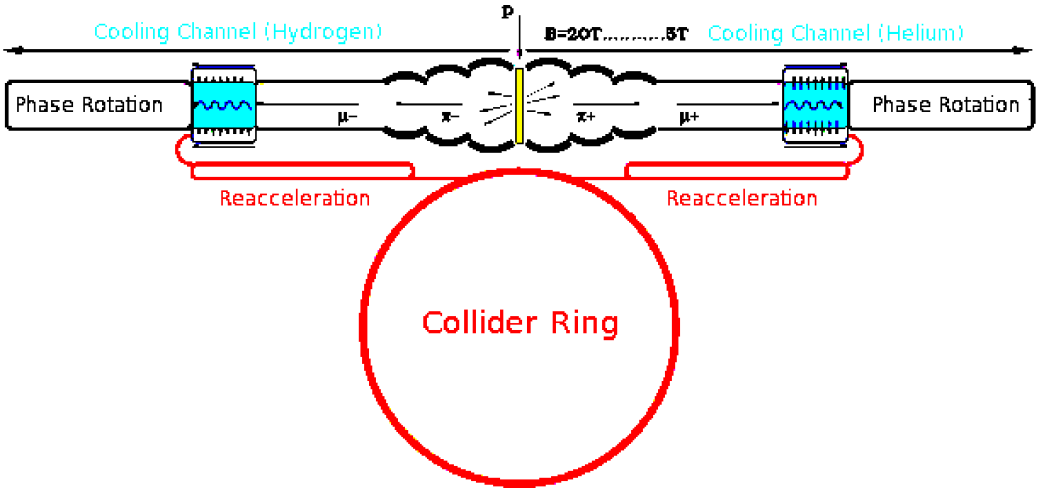

Figure 5.1: Schematic layout of a Muon Collider structure (not to scale).

The phase rotation section is also already implemented in the simulation program. But, corresponding simulation runs have not been performed yet.

After extraction from the cooling channel the low-emittance muons are reaccelerated in vacuum until they are finally inserted into the Muon Collider ring. This procedure is valid for positively and negatively charged muons as outlined in fig. 5.1 so that a $\mu^+\mu^-$ collider is conceivable [4]. In the following, the discussion is centered on the muon cooling channel. Its properties are presented and simulation results are given and interpreted.

5.2 Muon Cooling

5.2.1 The Channel

The muon cooling channel consists of a tube, 11 m in length and 40 cm in diameter, filled with either Helium for the cooling of μ^+ or Hydrogen for the cooling of μ^- (see discussion in chapter 3). Lower densities are favorable since they allow for lower electric field strengths used with Frictional Cooling (see fig. 4.21) which reduces the probability of space charge effects and electrical breakdowns. On the other hand, lower densities imply a longer gas cell to achieve the same cooling effect since muons experience a smaller energy loss due to the retarding medium.

The cooling scheme is able to cool muons in the range of several MeVs to several 100 of MeVs of total momentum. To be able to apply the principle of Frictional Cooling the muons first have to be slowed down below the crossing

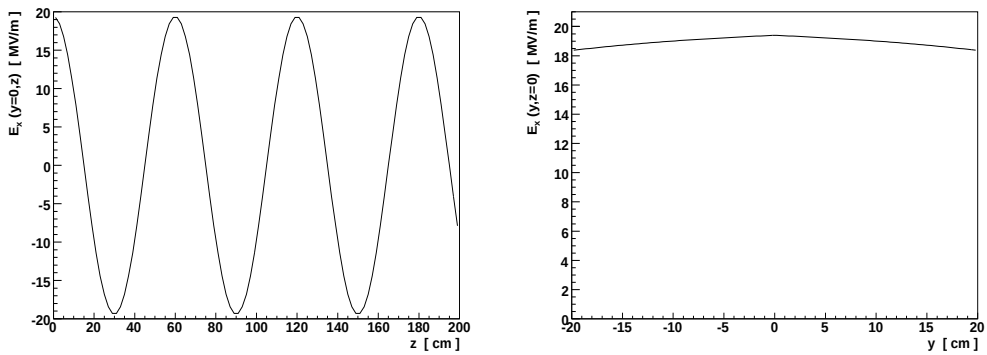

Figure 5.2: The electric field $E_x(y, z)$ used in the simulation of the muon cooling channel, depending on z for $y = 0$ (left) and on y for $z = 0$ (right).

point of stopping power and electric field on the right side of the ionization peak (see fig. 2.1 and fig. 3.1). This is done by applying crossed electric and magnetic fields. The principle field configurations are taken from [4] even though the magnitudes where changed in the present simulation.

The magnetic field $\vec{B}(\vec{x})$ is constant and aligned along the z-axis and can be expressed as

$$\vec{B}(\vec{x}) = B_0 \cdot \hat{z} \tag{5.3}$$

where $B_0 = 5$ T and $\hat{z}$ is the unit distance vector along the z-axis. The electric field varies along the z-axis in the x direction perpendicular to the magnetic field. Furthermore, an exponential fall off depending on y is assumed. The electric field $\vec{E}(\vec{x})$ can be expressed as

$$\vec{E}(\vec{x}) = E_0 \cdot \cos(z \cdot \pi/\alpha) \cdot (1 - \exp\{(|y| - \beta)/\gamma\}) \cdot \hat{x} \tag{5.4}$$

with $E_0 = 20$ MV/m and $\hat{x}$ the unit distance vector along the x-axis. The parameters are chosen such that the electric field oscillates as a cosine function every $\alpha = 30$ cm and is exponentially damped at a radius of $\beta = 70$ cm. The gas cell has a radius of $\gamma = 20$ cm. The electric field is shown in fig. 5.2. For the effective Lorentz-Force from eq. (3.7) follows

$$\begin{aligned} \vec{F}_{\mathrm{L,eff}}(\vec{x}) &= q_{\mathrm{eff}}(T) \cdot q \cdot [\, E_0 \cdot \cos(z \cdot \pi/\alpha) \cdot (1 - \exp\{(|y| - \beta)/\gamma\}) \cdot \hat{x} \\ &+ B_0 \cdot (\dot{y}\hat{x} - \dot{x}\hat{y}) \,] \end{aligned} \tag{5.5}$$

which is used in the simulation of the muon cooling channel. Therefore, large oscillations of muons in the y-direction due to the Lorentz-Force are

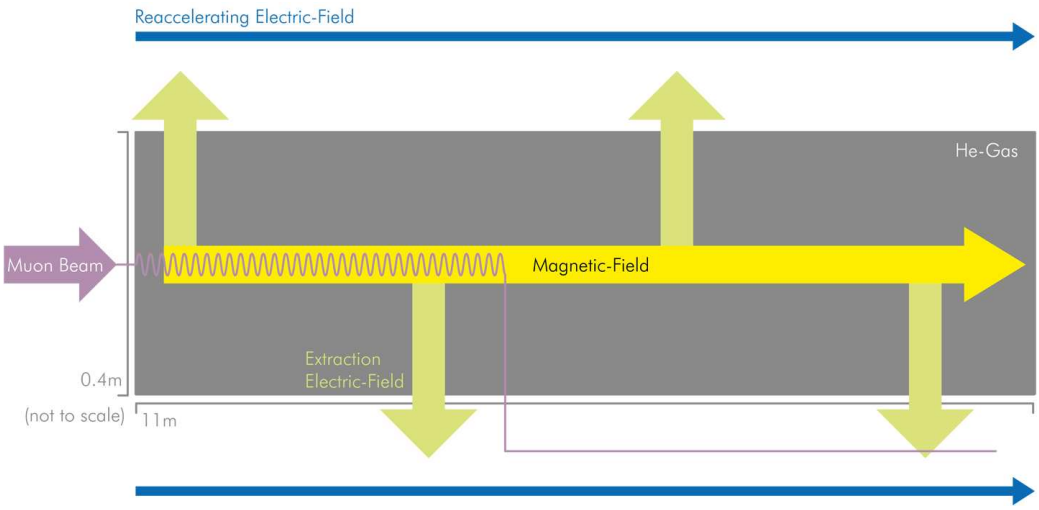

Figure 5.3: Schematical setup of the muon cooling channel including a typical muon trajectory.

expected. However, the magnetic field from eq. (5.3) will lead to a high-frequency circular movement, and thus, to a much larger path that muons travel which results in a strongly increased energy loss due to the retarding medium.

Therefore, the kinetic energies of the muons are reduced until they reach the Frictional Cooling regime. Once in this region muons will reach equilibrium energies and are extracted sideways at the so called Lorentz-Angle (see further discussions). Depending on their initial momenta they leave the gas cell at different z. Faster muons, as opposed to slower muons, need more time to be brought below the ionization peak. The overall setup and a schematical muon trajectory can be seen in fig. 5.3. An electric field along the z-axis outside of the gas cell will reaccelerate the muons after extraction.

5.2.2 Single Particles

In order to reach equilibrium energies in the Frictional Cooling regime for μ^+ and μ^-, Helium and Hydrogen are used at a density of 0.125 mg/cm^3. Generally, as shown in the previous chapter, the equilibrium energy only depends on density of the retarding medium and the strength of the electric field. However, here two particles with different stopping power curves in distinct gases (see fig. 3.1) are compared.

In fig. 5.4 the trajectories of single muons traversing through the gas cell

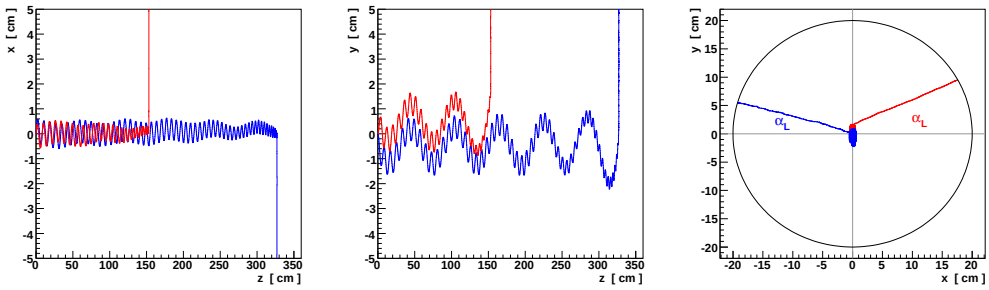

Figure 5.4: Trajectories of single muons traversing through the gas cell for μ^+ in Helium (blue) and μ^- in Hydrogen (red).

are shown for a typical initial momentum vector $\vec{P}_0$ of

$$\vec{P}_0 = (7, 0, 20) \text{ MeV/c} \tag{5.6}$$

The oscillations of the muons due to the Lorentz-Force can be clearly seen. Their movement can be described as a helix. Only those muons are accelerated sufficiently and survive the cooling section that are extracted around the maximum of the cosine behavior of the electric field along the z-axis.

One the right side of fig. 5.4 the orthogonal extraction of the muons respective to the z-axis can be clearly observed. The angle under which they leave the cell to the side respective to the x-axis (direction of the electric field) is called the Lorentz-Angle α_L. A common parametrization of the Lorentz-Angle [28, 29] is

$$\tan \alpha_\mathrm{L} = \psi \frac{B_0}{E_0} w^0 \tag{5.7}$$

where ψ denotes the dimensionless magnetic deflection coefficient (usually close to one) and w^0 the drift velocity in the absence of a magnetic field that only depends on density and electric field strength. A simulation run with zero magnetic field yielded $w^0 = 0.09$ cm/ns for μ^+ in Helium. Thus, using $\psi = 1$ eq. (5.7) yields to a Lorentz-Angle of

$$\alpha_\mathrm{L} = -0.23 \text{ rad} = -13.3^o \tag{5.8}$$

In fig. 5.5 the development of the kinetic energies for single muons is presented. Positively as well as negatively charged muons end up with similar equilibrium energies in the Frictional Cooling region. The equilibrium energy can be observed at approximately 1.4 keV for μ^+. Furthermore, the cooling process is rather short with approx. 0.3 μs compared to the lifetime of the

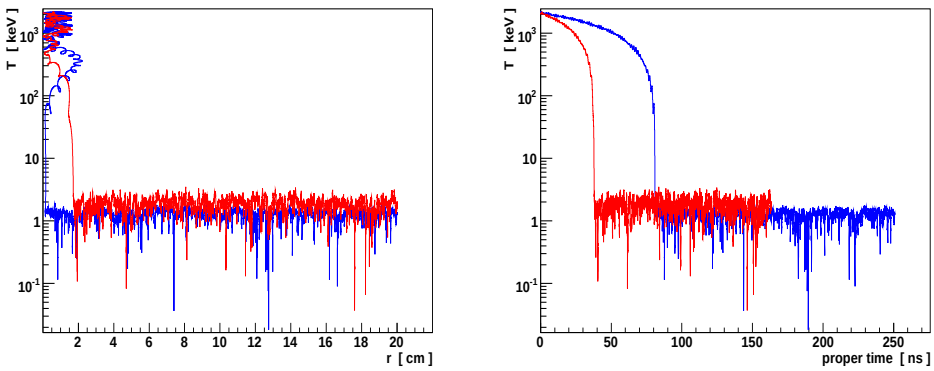

Figure 5.5: Development of the kinetic energy T of single muons traversing through the gas cell for μ^+ in Helium (blue) and μ^- in Hydrogen (red).

muon of 2.2 μs. Thus, it is expected to see large yields for μ^+ but less for μ^- due to the muon capture process (see chapter 3).

When muons begin to drift orthogonal to the z-axis they have energies below the ionization peak of the stopping power curve. Thus, from there on, until they are extracted, they only experience the exponential variation depending on y of the electric field from eq. (5.4) and the magnetic field which leads to the Lorentz-Angle from eq. (5.7). Therefore, the process of extraction is the application of the principle of Frictional Cooling. It is analog to the Frictional Cooling demonstration experiment.

Fig. 5.6 shows the three-dimensional trajectory of a positively charged muon traversing though Helium (produced by the graphics engine of Geant4) with the same conditions as above. The directions of electric field $\vec{E}$ and magnetic field $\vec{B}$ are outlined. The helical movement of the muon (blue) can be clearly seen. The red objects are electrons created because of the ionization of Helium atoms due to the muon incident. These so called delta-electrons are usually stopped after some mm due to interactions with the Helium atoms. Besides ionization, also excitation and nuclear energy loss contribute to the total energy loss.

Right before the muon starts to drift along the Lorentz-Angle the most electrons are created since the muon's kinetic energy is in the region of the ionization peak in the stopping power curve. While drifting ionization still gives the largest contribution to the well simulated energy loss unless no electrons are visible anymore. This is due to a nonphysical production threshold of secondary particles at lower energies in the Geant4 framework.

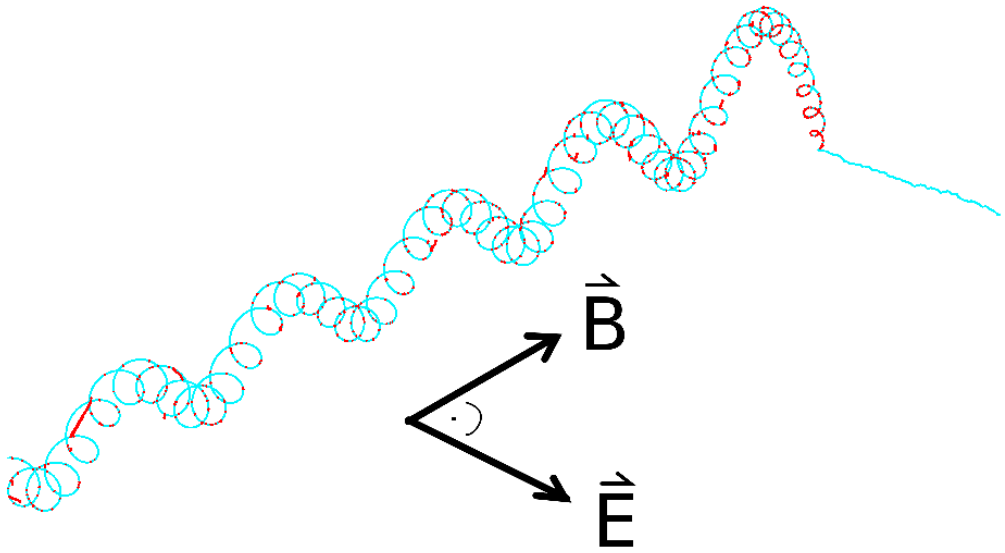

Figure 5.6: Three-dimensional trajectory of a positively charged muon (blue) traversing though Helium. Electric field $\vec{E}$ and magnetic field $\vec{B}$ are outlined. The red objects indicate electrons from ionization processes.

5.2.3 Equilibrium Energy

In order to estimate the expected equilibrium energy range of the muons right before leaving the gas cell sideways, the continuous energy loss approximation is applied and eq. (4.4) using eq. (5.5) is solved with a 4th-order Runge-Kutta-Method. As in chapter 4, it is assumed that the muons are not laterally displaced. Furthermore, the muons shall only travel parallel to the x-axis, and so experience the full electric field strength because of $\alpha_L = 0$.

The results for μ^+ in Helium are shown in fig. 5.7 for various densities. The equilibrium energies are reduced by a factor of approximately $m_\mathrm{p}/m_\mu = 8.87$ (velocity scaling) compared to those of protons in Helium. Exemplary, for $E_0 = 20$ MV/m and a density of 0.125 mg/cm^3, the positively charged muons end up at an equilibrium energy of

$$T_\mathrm{eq} \approx 1.5 \text{ keV} \tag{5.9}$$

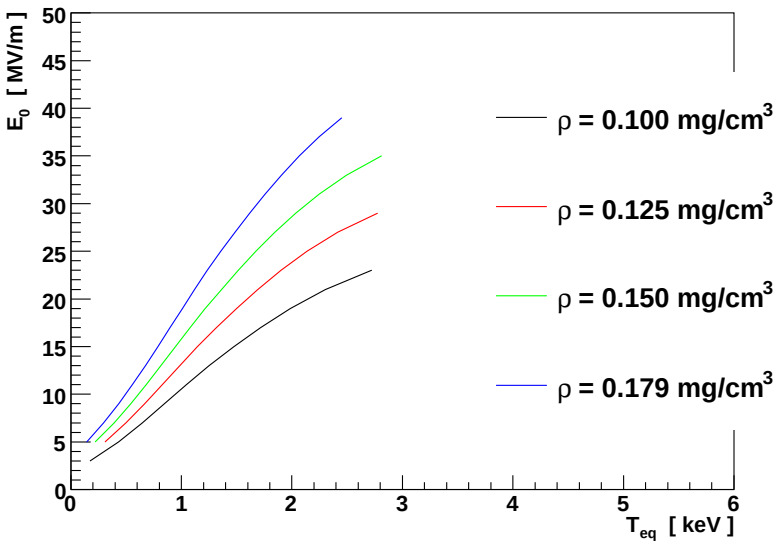

Figure 5.7: E_0 versus the equilibrium energy for various densities calculated with a Runge-Kutta-Method for μ^+ in Helium at $\alpha_{\mathrm{L}} = 0$.

5.2.4 A Muon Beam

In order to achieve realistic results a typical muon beam with a high spread in momentum and 10,000 particles is simulated. In the following, μ^+ in Helium is outlined in blue and μ^- in Hydrogen in red. Both gases have a density of 0.125 mg/cm^3. Muons entering the cooling channel are sampled on a circle with a radius of 5 cm. Fig. 5.8 shows the initial spatial distributions. The distributions of muons that are successfully cooled and extracted from the cooling channel are shaded.

The muon bunches for both, μ^+ and μ^-, have an initial Gaussian distribution in kinetic energy with a mean of 4 MeV and a standard deviation of 1 MeV. The distributions in total momentum of muons entering the cooling channel is shown in fig. 5.8 as well. The distributions of successfully cooled muons are shaded. The yield for μ^+ in Helium is 7.2 % whereas that of μ^- is 7.1 %. Due to the process of muon capture that μ^- additionally experience, one might expect a significantly lower yield for μ^-. But, the effective charge leads to a lower energy gain of μ^+ from the electric field which significantly reduces the yield of μ^+. Also, they need more time to be cooled which leads to more decays compared to μ^-. It can be stated that the yields for both, particle and anti-particle, are approximately equal.

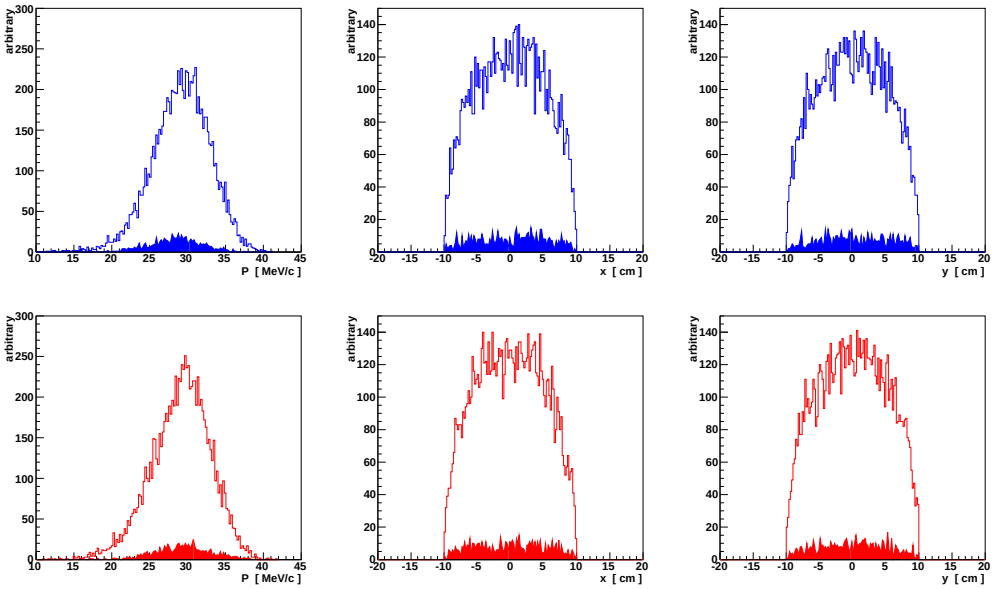

Figure 5.8: Initial total momentum and spatial distributions of muons entering the cooling channel. Muons that are successfully cooled and extracted are shaded.

The initial momentum components of the beam before it enters the cooling channel are shown in fig. 5.9. In the same figure the resulting distribution of extracted muons for each momentum component are shown as a filled area. The spread in momentum is very strongly reduced. A large cooling effect in all momentum components can be observed. Please refer to the next subsection for a calculation of the transverse emittance.

In fig. 5.10 the distributions in kinetic energy T, Lorentz-Angle α_{L}, and proper time t_{P} right before extraction of the muons are shown. The μ^+ end up with an equilibrium energy of 1.42 keV. This is in good agreement with the results from the continuous loss approximation for the equilibrium energy given in eq. (5.9). Thus, it is assumed that the simulation results are reliable.

Furthermore, fig. 5.10 shows that the μ^+ are extracted under a Lorentz-Angle of -0.36 rad which corresponds to -20.6^o. The previous calculation given in eq. (5.8) yielded a Lorentz-Angle of -13.3^o. Thus, the magnetic deflection coefficient ψ introduced in eq. (5.7) is estimated as

$$\psi = 1.59 \tag{5.10}$$

However, it will be a future experimental task to determine ψ for different sets of conditions.

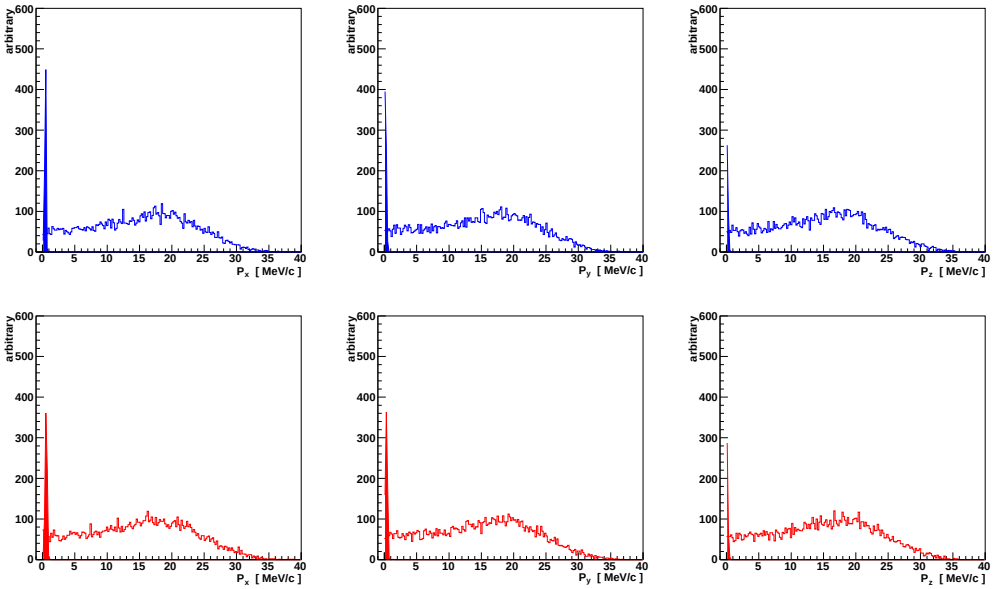

Figure 5.9: Initial momentum components of muons entering the cooling channel (lines) and final momentum components (filled area).

The spreads in energy and angle are rather small whereas the spread in proper time becomes large. The latter one represents the increased spread in z due to multiple scattering and the large initial momentum spread.

The maximum time the muons need to be cooled is approximately $t_{\mathrm{p,max}} =$ 400 ns which is still a factor of 5 smaller than their mean lifetime of 2200 ns. It is not expected to loose many particles due to their decay. Therefore, space charge effects in the cooling channel due to free electrons from the decay of muons can be neglected with the current setup. However, larger initial momenta would lead to greater times the muons need to be cooled and extracted.

Fig. 5.10 also shows the results for μ^-. Due to the higher stopping power and the higher energy gain (no effective charge) the μ^- experience they need less time for being extracted, but additionally, the spread around the equilibrium energy is larger than for μ^+ in Helium.

The average Lorentz-Angle under which the μ^- are extracted is 0.52 rad which corresponds to 29.8^o. This angle is positive, in contrast to α_L for μ^+, due to the opposite charge of μ^-. The difference in magnitude appears because of the different stopping power in Hydrogen and a higher energy gain. The higher acceleration the μ^- experience in comparison to μ^+ leads

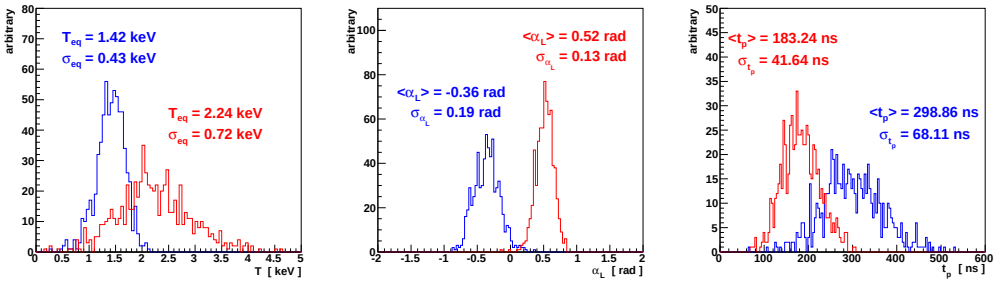

Figure 5.10: Distributions in kinetic energy T (left), Lorentz-Angle α_L (middle) and proper time t_P (right) of muons right before extraction.

to a higher equilibrium energy of $T_{\text{eq}} = 2.24$ keV.

5.2.5 Luminosity

The average transverse emittance was calculated using eq. 1.2. This calculation does not take any correlations between the evaluated distributions into account. Therefore, this estimate is conservative because any correlations between the variables would decrease the emittance. The initial and final values of the standard deviations for the four-dimensional ingredients of the transverse emittance and the ϵ_T itself are outlined in fig. 5.11. A transverse emittance reduction by two orders of magnitude can be observed. The reduction is mainly due to a very strong compression in all momentum components, and therefore, due to the large reduction of the spread in kinetic energy. But, also the spatial transverse spread could be reduced by a factor of two.

Both beams of μ^+ and μ^- have reached equilibrium energies in Helium and Hydrogen. The average transverse emittance could be reduced significantly. The concept of Frictional Cooling could be successfully applied.

The luminosity L, as defined in eq. (1.1), is calculated for reasonable collider parameters while using the emittance ϵ_T calculated in fig. 5.11 .

	μ^+ in Helium	μ^- in Hydrogen
σ_x^0 [cm]	4.99	4.98
σ_y^0 [cm]	5.02	5.03
$\sigma_{p_x}^0$ [MeV/c]	7.86	7.96
$\sigma_{p_y}^0$ [MeV/c]	7.93	7.97
ϵ_T^0 [cm]	$1.19 \cdot 10^{-1}$	$1.20 \cdot 10^{-1}$
σ_x [cm]	3.87	2.64
σ_y [cm]	3.88	2.65
σ_{p_x} [MeV/c]	0.11	0.14
σ_{p_y} [MeV/c]	0.13	0.15
ϵ_T [cm]	$1.40 \cdot 10^{-3}$	$1.14 \cdot 10^{-3}$

Figure 5.11: Initial and final values of the standard deviations for the ingredients of the average transverse emittance ϵ_{T}.

Typical parameters of a possible Muon Collider are [30]

$$\begin{aligned} \text{COM energy} &= 3 \text{ TeV} \\ \text{Collider circum.} &= 6000 \text{ m} \\ \text{proton energy} &= 16 \text{ GeV} \\ \text{proton power} &= 28 \text{ MW} \\ \mu/\text{bunch} &= 2 \cdot 10^{12} \\ \text{No. of bunches} &= 4 \\ \beta^* &= 0.3 \text{ cm} \end{aligned}$$

Therefore, for an average transverse emittance of $\epsilon_T = 10^{-3}$ cm the luminosity calculation yields

$$L = 2 \cdot 10^{32} \text{ cm}^{-2}\text{s}^{-1} \tag{5.11}$$

This is two orders of magnitude lower than the final beam luminosity of the LHC. In order to reach this goal, other parts of the cooling system will contribute to the overall emittance reduction: the reacceleration stage [4], phase rotators and bunchers [1] as well as the final beam compression in the actual collider ring.

5.3 Challenges

Many problems need to be solved until a Muon Collider can be build. One of them was addressed in this work, the cooling of a beam of muons. It was shown that free electrons inside the cooling channel due to the decay of muons are not significant. However, the issue of free charges, electrons and ions, due to ionization processes needs further research since they could screen the electric field or lead to electrical breakdowns. The simulation has shown that a beam in the $20-30$ MeV/c range of total momentum produces approximately 1000 electrons and thus, another 1000 ions per track. The number of muons per bunch in the collider should be $2 \cdot 10^{12}$. If a realistic yield of 5 % in the muon cooling channel (including phase rotation and reacceleration) is assumed then at least $4 \cdot 10^{12}$ need to enter the cell, leading to $8 \cdot 10^{15}$ free charges. The question is if these charges may exist at the same time and build up regions of space charges.

Another issue connected to the latter one is the overall yield of muons from the pion production target to the final injection in the Muon Collider ring. A small percentage of muons surviving this path would not be a problem if enough muons were produced, implying that the energy of the proton driver must be high enough (at least several GeV).

It will be a challenge in particular to develop ultra-thin windows that are able to let pass the muons during extraction from the cooling channel with minimum losses of energy. Note that cooled muons exiting the channel will not have energies greater than 4 keV.

The energy loss and scattering processes in the low-energy regime need further research. It is necessary to determine the corresponding cross-sections for muons in various gases experimentally. Because both, muons and protons, are heavy charged particles, the Frictional Cooling demonstration experiment with protons aims to understand these processes. It was also proposed to move the FCD experiment to the Paul-Scherrer-Institute in Villigen, Switzerland, since they provide low-energy muon beams. Here, also the capture of negatively charged muons by medium atoms below 1 keV could be investigated. Currently, only theoretical predictions are available in this region.

Chapter 6

Conclusions

The Monte Carlo simulation based on the Geant4 framework was successfully validated. The simulation is able to produce reliable predictions. It was shown that Geant4 is able to efficiently simulate the energy loss of protons and muons traversing through Helium and Hydrogen. The effects of electric and magnetic fields were shown. The influence of an effective charge of protons and positively charged muons on the Lorentz-Force was described. All future simulations of Frictional Cooling have to take this into account. Also, muon capture by medium atoms was considered and implemented in the simulation.

The FCD experiment currently developed at the Max-Planck-Institute for Physics in Munich will be able to demonstrate and prove the principle of Frictional Cooling. Predictions for kinetic energies of protons in the detector were made. The achievable balance of the energy loss due to the retarding medium and the energy gain due to an effective electric field could be presented. It was shown that the usage of multi-energetic proton sources would fully demonstrate the principle of Frictional Cooling. If construction constraints can be overcome and a high activity proton source will be used the FCD experiment will be able to measure protons at high data rates and acceptance in the detector.

The connection between the demonstration experiment and the muon cooling channel in a possible Muon Collider structure was given. The setup of the muon cooling channel including gas properties, geometry and electromagnetic fields was introduced. Simulation results have shown that muons with several MeV initial kinetic energy can be cooled and extracted sideways out of the gas cell. They leave the cell under the Lorentz-Angle which does not depend on the muons initial momentum components. Only its charge, the density of the gas, the electric field strength as well as the magnetic field strength affect the value of the Lorentz-Angle.

It was shown that the emittance, and thus, the occupied phase space volume of a muon beam can be significantly reduced. Furthermore, this is achievable on a timescale smaller than the lifetime of the muon. The luminosity was determined to be promising but not high enough. However, Frictional Cooling can be an important part of a cooling scheme used in a possible Muon Collider structure. It is conceivable to use existing colliders like the LHC or LEP to make a Muon Collider possible.

The simulation results have to be validated by data from the FCD experiment. First runs with protons traversing through Helium and a running accelerating grid are planned for the beginning of 2009.

The next steps in enhancing the simulation are: performing simulation runs including the phase rotation section and a muon beam at higher total momenta (mean around 100 MeV/c), implementing the reacceleration stage and finally, developing methods that simulate the pion production and drift in the pion decay channel.

References

[1] K. Paul et al. Summary of the low-emittance muon collider workshop. *Linear Colliders, Lepton Accelerators and New Acceleration Techniques*, A09:2412–2414, February 2006.

[2] J. L. Hirshfield. Electron-beam cooling by stimulated synchrotron emission and absorption. *Phys. Rev. Lett.*, 66(18):2312–2315, 1991.

[3] S. van der Meer. Stochastic cooling and the accumulation of antiprotons. *Rev. Mod. Phys.*, 57:689–697, 1985.

[4] A. Caldwell et al. A muon collider scheme based on frictional cooling. *Nucl. Instr. and Meth. A*, 546:356–375, 2005.

[5] S. Ozaki et al. Feasibility Study-II of a muon-based neutrino source. Technical report, BNL, June 2001. 52623.

[6] E. Morenzino. Physics and applications of low energy muons. *Muon Science*, 1999.

[7] M. Mühlbauer et al. Frictional cooling: latest experimental results and first application. *Nucl. Phys. B*, 51A:135–142, 1996.

[8] R. Galea et al. A frictional cooling demonstration experiment with protons. *Nucl. Instr. and Meth. A*, 524:27–38, 2004.

[9] National Institute for Standards and Technology. *ICRU Report 49*. NIST, 1994.

[10] B. H. Bransden. The interaction of positively charged muons with atomic hydrogen at low energies. *J. Phys. B: At. Mol. Opt. Phys.*, 23:115–119, 1990.

[11] W.-M. Yao et al. Passage of particles through matter. *J. Phys.*, G 33, 2006.

[12] J. F. Ziegler et al. *The Stopping and Range of ions in matter.* SRIM, 2008.

[13] S. Agostinelli et al. Geant4 - a simulation toolkit. *Nucl. Instr. and Meth. A*, 53:270–278, Feb. 2006.

[14] http://geant4.cern.ch. *Geant4 Physics Reference Manual.*

[15] S. Chauvie et al. Geant4 low energy electromagnetic physics. *Proc. IEEE Nuclear Science Symp. Conf. Rec.*, 3:1881–1885, Oct. 2004.

[16] V. N. Ivanchenko. Geant4 simulation of energy losses of ions. *CERN-OPEN-99-300*, 1999.

[17] S. Giani et al. Geant4 simulation of energy losses of slow hadrons. *INFN/AE-99/20*, 1999.

[18] A. G. Bogdanov et al. Geant4 simulation of production and interactions of muons. *IEEE Transactions on nuclear science*, 53 No. 2, April 2006.

[19] L. Urban. Multiple scattering model in Geant4. *CERN-OPEN-2002-070*, 2002.

[20] Y. Nakai et al. Cross sections for charge transfer of hydrogen atoms and ions colliding with gaseous atoms and molecules. *Atomic Data and Nuclear Data tables*, 37:69–101, 1987.

[21] C. Amsler et al. Particle data group. *Phys. Lett.*, B667, January 2008.

[22] J. S. Cohen. Multielectron effects in capture of antiprotons and muons by helium and neon. *Phys. Rev. A*, 62:022512, July 2000.

[23] J. S. Cohen. Fermion molecular dynamics in the capture of muons by hydrogen atoms. *J. Phys. B: At. Mol. Opt. Phys.*, 31:L833–L840, August 1998.

[24] SIMION, Scientific Instruments Services, Inc., www.simion.com.

[25] R. Keys. Cubic convolution interpolation for digital image processing. *EEE Transactions on Signal Processing, Acoustics, Speech, and Signal Processing*, 29, 1981.

[26] J. D. Jackson. *Classical Electrodynamics.* Wiley, 1999.

[27] D. E. Greenwald. Characterization of the proton source in the frictional cooling demonstration experiment. Diplomarbeit, Technical University of Munich (TUM), 2008.

[28] T. Kunst et al. Precision measurements of magnetic deflection angles and drift velocities in crossed electric and magnetic fields. *Nucl. Instr. Meth.*, A324:127–140, 1993.

[29] K. Hoshina. A study of the lorentz-angle for JLC CDC. Master's thesis, Tokyo Univerity of Agriculture and Technology, 1999.

[30] C. M. Ankenbrandt et al. Status of muon collider research and development and future plans. *Phys. Rev. ST Accel. Beams*, 2:081001, 1999.

Acknowledgments

I would like to begin by thanking the people whom have supported me in not only my academic pursuits but in all my life decisions, my family. Without them this work would have not been possible and I am forever grateful to them for their support.

Warm acknowledgments to my professor Allen Caldwell whose guidance and support helped make this thesis all that it is. The Post Doctorate who brought me into the FCD experiment, Daniel Kollár who I was sad to see leave the assignment before my completion. Along with his replacement Guoxing Xia who joined in the latter of my research but influenced me greatly.

I wish to thank my fellow students who assisted me on my research; Daniel Greenwald, who provided me with motivation and insight on all aspects of our work and Bao Yu who joined the project the same time as me and proved to be helpful. And of course the Technical University of Munich where I completed my studies before joining the MPI.